Geophysical Journal International

Geophys. J. Int. (2015) **201,** 247–266 doi: 10.1093/gji/ggv012
GJI Marine geosciences and applied geophysics

Resistivity inversion in 2-D anisotropic media: numerical experiments

Timothy Wiese,[1] Stewart Greenhalgh,[2] Bing Zhou,[3] Mark Greenhalgh[4] and Laurent Marescot[5]

[1] *Oil Development Section, Santos Ltd,* 60 *Flinders Street, Adelaide* 5000*, South Australia*
[2] *Institute of Geophysics, ETH Zurich, Sonneggstrasse* 5*, Zurich* 8092*, Switzerland. E-mail: gstewart@aug.ig.erdw.ethz.ch*
[3] *Petroleum Geoscience Department, The Petroleum Institute, P.O. Box* 2533*, Abu Dhabi, UAE*
[4] *Thumping Geophysics, Great Eastern Highway, Rivervale* 6103*, Western Australia*
[5] *Risk Management Solutions, Stampfenbachstrasse* 85*, Zurich* 8021*, Switzerland*

Accepted 2015 January 6. Received 2015 January 6; in original form 2014 July 18

SUMMARY

Many rocks and layered/fractured sequences have a clearly expressed electrical anisotropy although it is rare in practice to incorporate anisotropy into resistivity inversion. In this contribution, we present a series of 2.5-D synthetic inversion experiments for various electrode configurations and 2-D anisotropic models. We examine and compare the image reconstructions obtained using the correct anisotropic inversion code with those obtained using the false but widely used isotropic assumption. Superior reconstruction in terms of reduced data misfit, true anomaly shape and position, and anisotropic background parameters were obtained when the correct anisotropic assumption was employed for medium to high coefficients of anisotropy. However, for low coefficient values the isotropic assumption produced better-quality results. When an erroneous isotropic inversion is performed on medium to high level anisotropic data, the images are dominated by patterns of banded artefacts and high data misfits. Various pole–pole, pole–dipole and dipole–dipole data sets were investigated and evaluated for the accuracy of the inversion result. The eigenvalue spectra of the pseudo-Hessian matrix and the formal resolution matrix were also computed to determine the information content and goodness of the results. We also present a data selection strategy based on high sensitivity measurements which drastically reduces the number of data to be inverted but still produces comparable results to that of the comprehensive data set. Inversion was carried out using transversely isotropic model parameters described in two different co-ordinate frames for the conductivity tensor, namely Cartesian versus natural or eigenframe. The Cartesian frame provided a more stable inversion product. This can be simply explained from inspection of the eigenspectra of the pseudo-Hessian matrix for the two model descriptions.

Key words: Inverse theory; Electrical properties; Electromagnetic theory.

1 INTRODUCTION

Resistivity tomography is widely used as an effective underground exploration technique in a variety of near-surface applications, including mineral search, civil engineering site investigations, groundwater hydrology and contaminant investigations (Butler 2005; Rubin & Hubbard 2005; Reynolds 2009). Imaging can be conducted either from the surface or between boreholes, or a combination approach. Nearly all of the published examples assume electrical isotropy of the ground. This may seem rather surprising given the compelling field and laboratory evidence that many rocks have a clearly expressed anisotropy (Maillet 1947; Keller & Frischknecht 1966; Parkomenko 1967; Bhattacharya & Patra 1968). The cause of this directional dependence in the resistivity can be microscopic in nature, for instance determined by intrinsic material properties such as platy mineral fabric or lineation, for example, clays. Anisotropy may also occur on a macroscopic scale whereby a series of layers or bands of dissimilar isotropic materials behave as a single, equivalent anisotropic unit. Layering, fracturing, jointing or rock cleavage can all produce this type of structural anisotropy. Typical values of the coefficient of anisotropy λ (square root of the ratio of maximum to minimum resistivity—see eq. 4) for shale and sandstone interbeds are in the range 1.05–1.15. Coal typically has a value between 1.7 and 2.6 due to cleating, while interbedded anhydrite and shale have reported values of 4.0–7.5. Even alluvium can have anisotropy factors of 1.02–1.1 (Hill 1972; Asten 1974).

A detailed discussion on how to detect anisotropy from surface dc resistivity measurements is beyond the scope of this paper, but may be found in the article by Greenhalgh *et al.* (2010). It includes techniques such as azimuthal resistivity surveys (Watson & Barker 1999; Busby 2000), square electrode arrays (Habberjam 1975; Matias 2002) and tensor measurements (Caldwell & Bibby 1998; Bibby

et al. 2005). The diagnosis is often improved if cross-hole resistivity data is available or if electric induction logging can be carried out in boreholes (Lu *et al.* 2002).

There are four principal reasons why anisotropy is seldom incorporated into practical dc resistivity investigations: (1) the problem of electrical equivalence, which means that it is impossible to distinguish from scalar surface electrical measurements between horizontal layering and macro-anisotropy of the medium, (2) the paradox of anisotropy (Keller & Frischknecht 1966), whereby the apparent resistivity is lower in the resistive across-strike direction and higher in the conductive in-strike direction, frustrating attempts by the geophysicist to recognize the counter-intuitive effects of anisotropy, (3) the geoelectric field is static in nature and limited in resolution capability, especially with increasing distance/depth distance from the electrodes and (4) anisotropy means an increase in the number of parameters to be recovered from the data, for what is already an often seriously underdetermined inverse problem.

By contrast, anisotropy is often incorporated into diffusive (ac) field magnetotelluric investigations (Reddy & Rankin 1971; Loewenthal & Landisman 1973; Dekker & Hastie 1980; Everett & Constable 1999; Linde & Pedreson 2004; Wannamaker 2005; Collins *et al.* 2006) and electromagnetic (EM) induction surveying (Le Masne & Vasseur 1981; Yu & Edwards 1992; Slater *et al.* 1998; Yin & Fraser 2004). A similar paradox of anisotropy occurs for EM but there are procedures to resolve it (Gianzero 1999; Wang & Fang 2001; Weiss & Newman 2002; Al-Garnt & Everett 2003). A list of references on numerical modelling procedures for EM in the presence of anisotropy is given in the paper by Yin & Fraser (2004).

The literature on dc resistivity modelling incorporating anisotropy is comparatively rather sparse. The semi-analytic forward solutions for half-spaces, vertical contacts, layered media and prismatic bodies in an anisotropic background are reviewed by Greenhalgh *et al.* (2009a). For general heterogeneous, anisotropic media, three approaches have been used: the finite difference method (LaBreque *et al.* 2004), the finite element method (Pain *et al.* 2003; Li & Spitzer 2005) and the Gaussian quadrature grid method (Zhou *et al.* 2009).

There are just a handful of published papers on anisotropic resistivity inversion. LaBreque *et al.* (2004) incorporated anisotropy into the finite difference modelling formulation of Dey & Morrison (1979), but assumed that the axes of the conductivity ellipsoid were aligned with the co-ordinate directions, greatly simplifying the problem. They use an Occam-style inversion scheme with an objective function including regularization operators to control the smoothness and the magnitude of anisotropy permitted. Pain *et al.* (2003) used a Levenberg–Marquardt type iterative preconditioned conjugate gradient inverse solver and a finite element forward solver. Their major contribution was to formulate and incorporate penalty functions for anisotropy and structure within the inversion objective function. Simple synthetic models with pole–pole array data sets were used to validate the inversion routine and highlight the non-linear nature of the problem. Suites of inversions were run to select the optimal penalty functions to minimize data residuals. Herwanger *et al.* (2004) extended the analysis by presenting a case study in which cross-hole resistivity and seismic methods were used to independently recover anisotropic model parameters. A good agreement of spatial structures with high anisotropy was found between the two techniques. The other notable inversion papers are those of Kim *et al.* (2006) and Yi *et al.* (2011), who present a case study in which 2-D and 3-D cross-hole tomography was able to delineate subsurface cavities having isotropic electric properties situated in a highly anisotropic biotite-gneiss subsurface. The orientations of the anisotropy axes were assumed to be in-line with the measurement (Cartesian) frame, an often questionable assumption. Anisotropy penalty terms were added to the objective function along with spatially varying Lagrange multipliers which increased stability and resolution in the inversion process. Unfortunately, precise details on the forward and sensitivity calculations are not provided for this case study in either paper.

A key component of any local search minimization style inversion strategy is the ability to compute the Fréchet derivatives or sensitivity functions. Recently, Greenhalgh *et al.* (2009b) presented a general adjoint method for computing the dc resistivity sensitivity kernels in 2.5-D and 3-D anisotropic heterogeneous media. In a companion paper (Greenhalgh *et al.* 2009a) they give explicit expressions for the various sensitivity functions in homogeneous anisotropic media, and in other contributions (Wiese *et al.* 2009; Greenhalgh *et al.* 2010) the anisotropic sensitivities are computed for various electrode arrays and compared with the isotropic sensitivities, showing the dangers of making an isotropic assumption when the ground is anisotropic.

In this paper, we go the next step and perform a series of 2.5-D inversion experiments for point electrode sources in 2-D synthetic anisotropic models. We examine image recovery for isotropic blocks (inclusions) within an anisotropic background, as well as anisotropic blocks within an isotropic background, and see what is possible under favourable three-sided recording conditions (i.e. combination cross-hole/borehole to surface). The purpose of the paper is not to present an optimized anisotropic inversion code *per se* but rather to compare these solutions against the distorted images obtained by inverting the synthetic (anisotropic) data under the false assumption of medium isotropy everywhere, which is the usual approach. We investigate the effect of changes in the dip angle of the plane of isotropy and changes in the degree of anisotropy. Various pole–pole, pole–dipole and dipole–dipole data sets are investigated and evaluated from the accuracy of the inversion result, by eigenspectra analysis of the pseudo-Hessian matrix and the relative resolution plots. We also present a data selection strategy based on high sensitivity measurements which produces inversion products comparable to that of comprehensive data sets. Reconstruction is attempted on equivalent anisotropic models with model parameters described in different co-ordinate frames (Cartesian and the principal axes or eigenframe).

2 BACKGROUND THEORY

2.1 2-D TI media

In its most general form, electrical anisotropy is described by a symmetric, second rank conductivity tensor with six independent components (Greenhalgh *et al.* 2009b). In this paper, we consider a more specific but prevalent class of anisotropy, that of a 2-D tilted transversely isotropic (TTI) medium involving just three independent components of the tensor (see Fig. 1a). In this model resistivity is equal in all directions within a specific plane termed the plane of isotropy (e.g. plane of stratification or foliation) but different in all other directions outside that plane. In optics, when dealing with the dielectric or refractive index tensor, this particular class of anisotropy is referred to as uniaxial and many minerals conform to it.

Here we will consider 2.5-D modelling which entails a point source of current and a 2-D model in which the resistivity parameters do not change in the y-direction or strike direction. The TTI model properties may be described with reference to

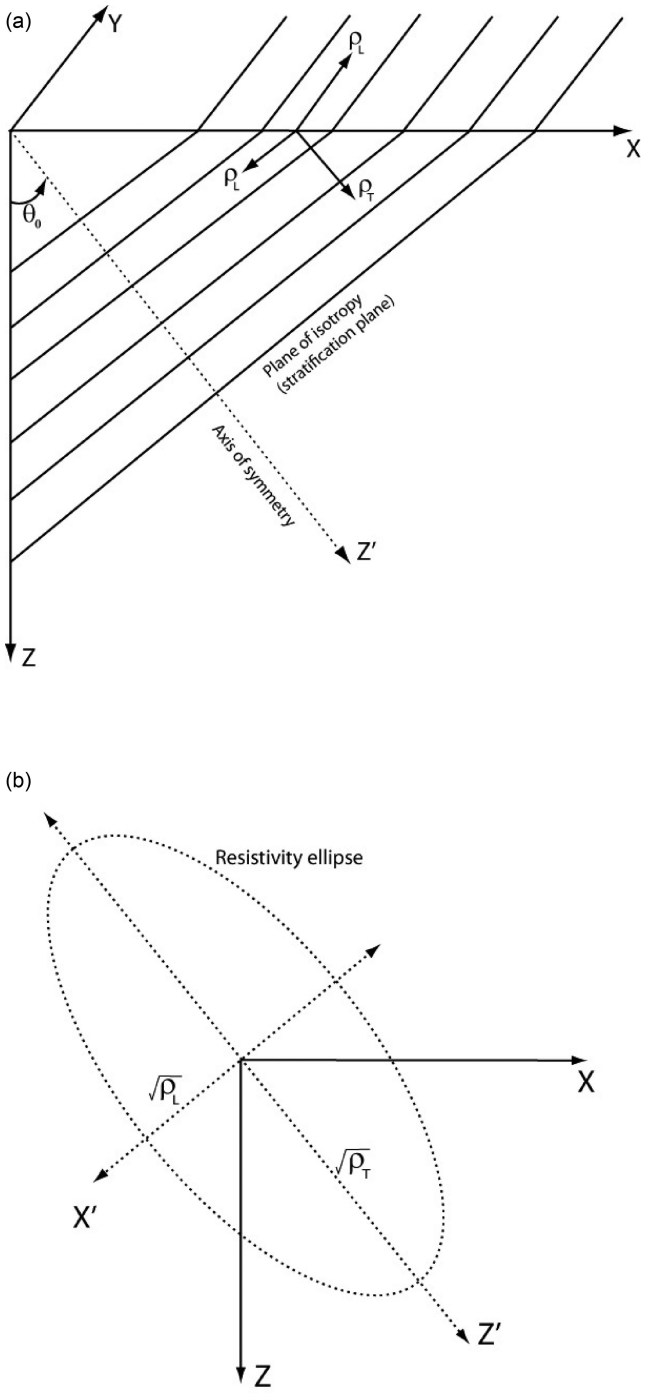

Figure 1. (a) Simplified diagram of anisotropic 2-D TTI media, showing axis of symmetry and principal resistivities. (b) The resistivity ellipse shown in relation to the (a) the geographic co-ordinate frame (X, Z), and (b) in the principal axis frame (or natural rock frame) (X′, Z′). The lengths of the semi major axes are equal to the inverse square roots of the principal resistivities (or eigenvalues of the 2 × 2 resistivity matrix). The directions of the principal axes are the corresponding eigenvectors.

either a geographic (measurement) co-ordinate frame involving the tensor elements ρ_{XX}, ρ_{XZ}, ρ_{ZZ} or a principal axis frame (or eigen-axis frame) involving the components ρ_L, ρ_T and θ_0. Here ρ_L is the longitudinal resistivity, ρ_T is the transverse resistivity and θ_0 is the angle of the symmetry axis relative to the vertical that is the transverse (uniaxial) direction. The principal axis frame is physically meaningful since the eigenvectors are aligned with the natural rock frame. This is illustrated schematically in Fig. 1(b). The semi-major and minor axes of the resistivity ellipse correspond to the two eigenvectors, and their lengths a and b are related to the eigenvalues or principal values according to the relations:

$$a = \sqrt{\rho_T} \quad \text{and} \quad b = \sqrt{\rho_L}. \tag{1}$$

The third eigenvector is in the y or medium-invariant direction. The two co-ordinate systems are related in terms of a rotation matrix derived in Greenhalgh *et al.* (2009b):

$$\begin{pmatrix} \rho_{xx} \\ \rho_{yy} \\ \rho_{xz} \\ \rho_{zz} \end{pmatrix} = \begin{pmatrix} \rho_L \cos^2\theta_0 + \rho_T \sin^2\theta_0 \\ \rho_L \\ 0.5(-\rho_L + \rho_T)\sin 2\theta_0 \\ \rho_L \sin^2\theta_0 + \rho_T \cos^2\theta_0 \end{pmatrix}. \tag{2}$$

The above formulae may be used to transform from ρ_{XX}, ρ_{XZ}, ρ_{ZZ} to ρ_L, ρ_T, θ_0:

$$\begin{aligned} \theta_0 &= \tan^{-1}\left(\frac{-2\rho_{xz}}{\rho_{xx} - \rho_{zz}}\right) \\ \rho_L &= \frac{\cos^2\theta_0\rho_{xx} - \sin^2\theta_0\rho_{zz}}{\cos 2\theta_0} \\ \rho_T &= \frac{-\sin^2\theta_0\rho_{xx} + \cos^2\theta_0\rho_{zz}}{\cos 2\theta_0}. \end{aligned} \tag{3}$$

By rearranging the orthogonal anisotropic resistivity model parameters (ρ_L and ρ_T) we may introduce an alternative form of description for TTI media, namely, the mean resistivity ρ_m and the coefficient of anisotropy λ, given by:

$$\rho_m = \sqrt{\rho_L\rho_T}, \ \lambda = \sqrt{\rho_T/\rho_L}. \tag{4}$$

The (ρ_M, λ) description is particularly insightful when gauging or comparing the magnitude of electrical anisotropy (λ) in material media. The quantity ρ_m is the geometric mean of the longitudinal and transverse resistivities. It is equal to the measured apparent resistivity

$$\rho_a = \frac{KU}{I} \tag{5}$$

on the ground surface in a direction parallel to the stratification in a medium having a vertical axis of symmetry (e.g. horizontal beds) known as a VTI medium or in the strike direction for a medium having a horizontal axis of symmetry (e.g. vertically dipping beds) known as a HTI medium. In eq. (5) U is the potential difference, I is the current strength and K is the geometric factor for the electrode array. The paradox of anisotropy (Keller & Frischknecht 1966) is that the apparent resistivity measured transverse to the layering in a HTI medium is actually equal to the longitudinal resistivity and not the transverse resistivity. In its most general form for uniaxial systems, the apparent resistivity measured in any one of the three principal directions will be equal to the geometric mean of the true resistivities in the other two orthogonal directions.

For isotropic media, $\rho_m = \rho_L = \rho_T$, and $\lambda = 1$.

Many papers work with the conductivity tensor $\boldsymbol{\sigma}$ rather than the resistivity tensor $\boldsymbol{\rho}$. They are simple inverses of each other such that $\boldsymbol{\rho\sigma} = \mathbf{I}$, where $\mathbf{I}$ is the identity matrix. In terms of the principal values in the rotated co-ordinate frame:

$$\sigma_L = 1/\rho_L, \ \sigma_T = 1/\rho_T, \ \sigma_{yy} = \sigma_L = 1/\rho_L. \tag{6}$$

The Cartesian element components σ_{xx}, σ_{zz}, σ_{yy}, σ_{xz} obey identical equations to the resistivity components of eq. (2) if we replace the ρ_L and ρ_T terms by the principal conductivities σ_L and σ_T, respectively.

2.2 GQG forward modelling

An essential requirement of any inversion scheme is a forward solver to compute the theoretical model response. For a point source of current in a 2-D medium, the governing equations for this so-called 2.5-D problem may be written as (Zhou *et al.* 2009):

$$\begin{cases} \nabla \cdot (\boldsymbol{\sigma} \cdot \nabla \tilde{G}) + k_y^2 \sigma_{yy} \tilde{G} = -\frac{1}{2}\delta(r - r_s), & r = (x, z) \in \Omega, \\ (\boldsymbol{\sigma} \nabla \tilde{G}) \cdot \mathbf{n} + \nu \tilde{G} = 0, & r = (x, z) \in \Gamma, \end{cases} \tag{7}$$

Here $\boldsymbol{\sigma}$ is the Cartesian symmetric conductivity matrix described above, $\mathbf{n}$ is the unit normal vector to the boundary Γ, ν is a known function of the spatial coordinates and the conductivity and specifies the mixed boundary condition, r_s is the current point-source location, k_y is the wavenumber or spatial Fourier transform variable corresponding to the y-direction. The quantity $\tilde{G}$ is the spatially Fourier transformed Green's function, which is equal to the impedance (or resistance) U/I. It is simply the voltage response for a unit current injection.

Zhou *et al.* (2009) presented the Gaussian quadrature grid numerical scheme for 2.5-D dc resistivity modelling in which the variational principle was applied to (7) to reformulate the problem in functional (Ψ) form:

$$\begin{cases} \min\{\Psi(\tilde{G})\} \\ \Psi(\tilde{G}) = \frac{1}{2}\int_{\Omega} [\nabla \tilde{G} \cdot \sigma \cdot \nabla \tilde{G} + \sigma_{yy} k_y^2 \tilde{G}^2] \mathrm{d}\Omega + \int_{\Gamma} \nu \tilde{G}^2 \mathrm{d}\Gamma - \tilde{G}_s \cdot \end{cases} \tag{8}$$

Here $\tilde{G}_S$ is the value of the Green's function at the source position. The model is parametrized into subdomains which are populated with nodes distributed at Gaussian quadrature abscissae points and are assigned weights corresponding to their positions (see Fig. 2).

The key step is to calculate the values of the functional at the Gaussian quadrature abscissae, which involves sampling the model parameters, the Green's function and its gradient based on the grid. The forward modelling reduces to solving a linear equation system and accuracy increases by increasing the abscissae number (Gaussian order) per dimension in the subdomain (for details, see Zhou *et al.* 2009). The main advantages of the method are its ability to deal with a complex geological model involving anisotropy and an arbitrary surface topography, whilst retaining the computational advantages of the spectral element method, yet a complex mesh generator is not needed as in the FEM (Greenhalgh 2008).

2.3 Fréchet derivatives

The sensitivity (Fréchet derivative) gives the change in measured potential (or apparent resistivity) due to a perturbation of the model parameter in a particular model. It is an essential component of any local search minimization type inversion scheme (Greenhalgh *et al.* 2006). In a recent paper (Greenhalgh *et al.* 2009b), we developed a new formulation for the anisotropic sensitivities for both the 3-D and the 2.5-D problems. For the latter, the result can be stated as:

$$\frac{\partial G^s(r_p)}{\partial m_\upsilon} = -F_c^{-1}\left\{\left[\nabla \tilde{G}^s(r) \cdot \frac{\partial \boldsymbol{\sigma}}{\partial m_\upsilon}\right] \cdot \nabla \tilde{G}^p(r) + k_y^2 \frac{\partial \sigma_{yy}}{\partial m_\upsilon} \tilde{G}^s(r) \tilde{G}^p(r)\right\}. \tag{9}$$

This equation shows that sensitivity can be computed in terms of the source $\tilde{G}^s$ (current electrode s) and adjoint source $\tilde{G}^p$ (potential electrode p) Green's functions and their gradients, as well as the derivatives of the conductivity tensor with respect to the principal model values. Here F_c^{-1} is the inverse Fourier cosine transform with respect to wavenumber. The model parameter m_υ may assume any of the anisotropic model parameters in either the Cartesian or eigenframes, which for the 2.5-D TTI problem under consideration comprises ρ_{L}, ρ_{T}, θ_0 or ρ_{xx}, ρ_{xz} and ρ_{zz}. (Note that $\rho_{yy} = \rho_{\mathrm{L}}$). Explicit expressions for the derivative term $\partial\boldsymbol{\sigma}/\partial m_\upsilon$ may be found in Greenhalgh *et al.* (2009b). A comprehensive study into the various anisotropic sensitivity functions in homogeneous anisotropic media for various arrays is given in Wiese *et al.* (2009). In a companion paper (Greenhalgh *et al.* 2010), these sensitivities are compared with those for an isotropic medium and the prominent differences in both the sign and magnitude of the sensitivities highlighted, showing the dangers of using an isotropic assumption when inverting anisotropic data.

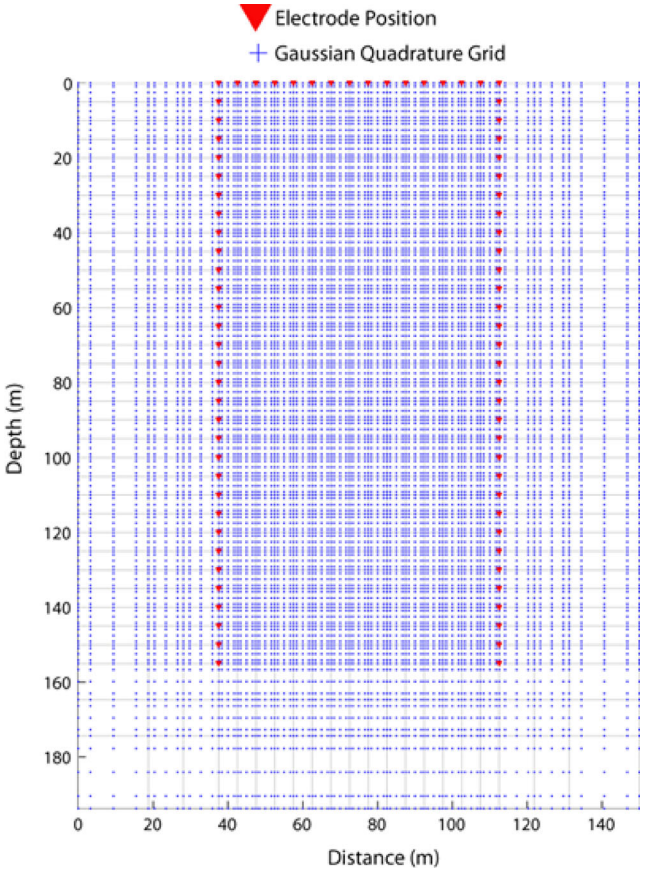

Figure 2. Blue crosses indicate the Gaussian quadrature grid of Gaussian order 5 used for forward modelling. The position of the 64 surface–borehole electrode array is shown by red dots.

Some authors express the isotropic sensitivities in a slightly different form than that used above (viz., $\partial G/\partial\sigma$), involving apparent resistivity ρ_a, or its logarithm $\log \rho_a$, or even in terms of resistance R, for example $\partial\rho_a/\partial\rho$, $\partial \log(\rho_a)/\partial \log(\rho)$, $\partial R/\partial\rho$. Conversion from one form to another is simple using implicit differentiation and the basic linking equations:

$$U = IG, \qquad \rho_a = KU/I, \qquad \boldsymbol{\sigma} = \boldsymbol{\rho}^{-1}. \tag{10}$$

The Jacobian matrix ($\mathbf{J} = \partial\mathbf{d}/\partial\mathbf{m}$, where $\mathbf{d} = \mathbf{U}$ or $\boldsymbol{\rho}_a$) is traditionally constructed with the rows related to the different measurement configurations and the columns corresponding to each model cell. The elements of the matrix are sensitivities, which are

dependent on the electrode configuration for the data point and the location of the model cell. In geo-electrics it is well documented that sensitivity decreases with distance from the electrodes because of the dc nature of the problem. Current lines are not straight, even in a homogeneous, isotropic medium.

2.4. Inversion approach

2.4.1. Gauss–Newton solution

Rather than building complicated smoothing and anisotropy penalty functions into the objective function, as has been previously done (e.g. Pain *et al.* 2003), here we concentrate on quantifying the effects of using an isotropic assumption to invert anisotropic data Comparisons between a (correct) anisotropic inversion with the isotropic reconstruction can only be done if the same inversion routine with similar regularization is used for both. For this reason the inversion scheme is chosen to be the well understood, widely used and easily implemented Gauss–Newton approach.

Central to any linearized least squares (or Gauss–Newton/Levenberg–Marquardt) inversion scheme is the forward operator (F) (GQG, see Section 2.2) used to calculate the synthetic or predicted data ($\mathbf{d}^{\text{pred}}$) which can be in the form of voltage or apparent resistivity for a given model ($\boldsymbol{m}$):

$$\mathbf{d}^{\text{pred}} = F(\mathbf{m}). \tag{11}$$

The inverse operator (F^{-1}) then seeks an estimate of the adjustments to the initial model parameters that best fit the observed data ($\mathbf{d}^{\text{obs}}$):

$$\Delta\mathbf{m}^{\text{est}} = F^{-1}(\mathbf{d}^{\text{obs}} - \mathbf{d}^{\text{pred}}). \tag{12}$$

The inverse operator may be written as an optimization (minimization) of an objective function (ϕ):

$$\min\{\varphi(\mathbf{m})\} = \min\{\varphi_d(\mathbf{m}) + \gamma\varphi_m(\mathbf{m})\} \tag{13}$$

γ is the damping factor that determines the trade-off between the data fit and the *a priori* knowledge on the model. The latter can be included through structural constraints, closeness to a preferred model or smoothing. Selection of the damping factor is discussed in Section 2.4.2.

The quantities ϕ_{d} and ϕ_{m} are the data and model misfit functions (or norms, respectively)

$$\phi_{\text{d}}(m) = \|W_{\text{d}}(d_{\text{obs}} - d(m)\|^2 \tag{14}$$

$$\phi_{\text{m}} = \|W_{\text{m}}(m - m_0)\|^2, \tag{15}$$

where m_0 is the starting or preferred model, and W_{m} and W_{d} are the model and data weighting matrices, respectively, for which various choices are available, depending on the definition of the solution (Greenhalgh *et al.* 2006). In this study, we set the weighting matrices W to the identity matrix I.

By calculating the derivatives of the data and model misfit functions we may derive the stationary point equation (Greenhalgh *et al.* 2006):

$$\gamma(\mathbf{m} - \mathbf{m}_0) = \left(\frac{\partial\mathbf{d}^{\text{pred}}}{\partial\mathbf{m}}\right)^T [\mathbf{d}^{\text{obs}} - \mathbf{d}^{\text{pred}}(\mathbf{m})]. \tag{16}$$

The stationary point equation may then be solved by an iteratively linearized scheme:

$$\mathbf{d}^{\text{pred}}(\mathbf{m}_{k+1}) \approx d^{\text{pred}}(\mathbf{m}_k) + \left(\frac{\partial\mathbf{d}^{\text{pred}}}{\partial\mathbf{m}}\right)_k [\mathbf{m}_{k+1} - \mathbf{m}_k)], \tag{17}$$

where $(\frac{\partial\mathbf{d}^{\text{pred}}}{\partial\mathbf{m}})_k$ is the Jacobian matrix ($\boldsymbol{J}_{\text{k}}$) at iteration k. The inverse operator can be written in Gauss–Newton form as:

$$\mathbf{m}^{\text{est}}_{k+1} = \left(\mathbf{J}_k^T\mathbf{J}_k + \gamma\mathbf{C}_m^{-1}\right)^{-1}\mathbf{J}_k^T\left[(\mathbf{d}^{\text{obs}} - \mathbf{d}^{\text{pred}}(\mathbf{m}_k)) + \mathbf{J}_k\mathbf{m}_k\right]. \tag{18}$$

Here C_{m} is the *a priori* model covariance matrix which allows regularization constraints such as smoothness (roughness), or minimum variation from some reference model. The resulting rectangular system can be solved by a conjugate gradient scheme (Greenhalgh *et al.* 2006).

2.4.2 Program description

The inverse problem requires that regularization be imposed to stabilize the solution and reduce the inherent non-uniqueness. It also helps to ensure that the inversion does not fall into a local minima but rather reaches the global minimum of the objective function

The damping factor choice specifies the trade-off between the pre-conceived ideas of the true model (*a priori* knowledge) and data fit. Smoothing was included through a finite difference operator that allowed variable weighting so that smoothness could be varied in different directions (deGroot-Hedlin & Constable 1990).

Since the experiments conducted were synthetic in nature without added noise (only numerical modelling errors were involved) the true model was known, making it possible to visually gauge the success of an inversion. A suite of inversions were carried out with various levels of damping. The inversions having the highest damping factor and which still converged to within numerical noise levels (<2 per cent) were selected for presentation. This way we neither oversmooth nor introduce false detail into the image. These inversions were the most optimal reconstructions of the true model with the least amount of artefacts. The inversion stopping criteria were that the desired data misfit of <2 per cent was reached (which we deemed to be below numerical noise inherent in our program), the number of iterations exceeded 20 or the difference between successive iterations produced an rms difference of less than 0.5 per cent. Convergence was calculated as the percentage ratio of the initial data misfit over the data misfit of the jth iteration. A flow chart showing the main elements of the inversion approach is given in Fig. 3.

2.4.3 Information content and resolution

The optimization of geophysical experimental design is an area of active and current research (Maurer & Boerner 1998; Stummer *et al.* 2004; Blome 2009; Loke *et al.* 2010, 2014; Maurer *et al.* 2010; Blome *et al.* 2011; Wilkinson *et al.* 2012), but compared to numerical forward modelling and inversion theory, this field of knowledge is far less developed.

Inversion algorithms are largely based on linearized theory (Menke 1989) and as such, methods for quantifying the benefits of a particular survey exist. The quality of an inversion result of a truly linear forward model can be appraised by examining the model resolution matrix formally defined as:

$$\mathbf{R} = \left(\mathbf{J}^T\mathbf{J} + \gamma\mathbf{C}_m^{-1}\right)^{-1}\mathbf{J}^T\mathbf{J}. \tag{19}$$

It relates the estimated model parameters to the true model parameters (m^{true}) through the equation:

$$\mathbf{m}^{\text{est}} \approx \mathbf{R}\mathbf{m}^{\text{true}}. \tag{20}$$

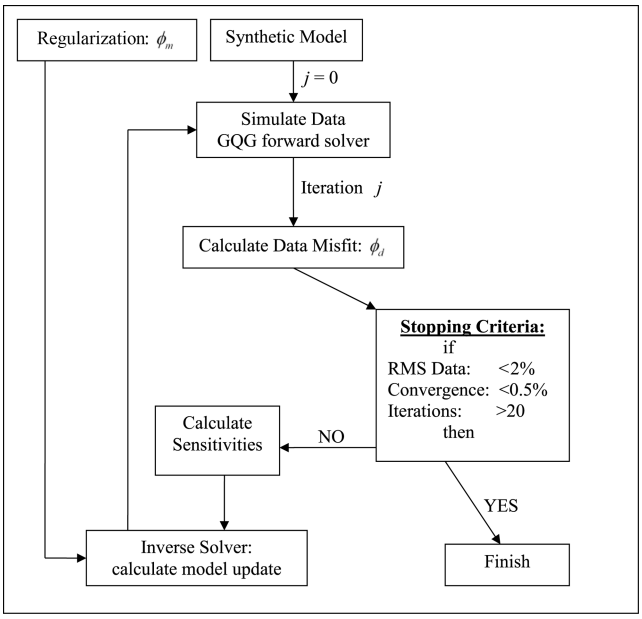

Figure 3. The inversion program flow chart shows the iterative methodology and convergence stopping criteria.

Of particular interest are the diagonal elements of $\boldsymbol{R}$. Values close to zero indicate poorly resolved model parameters, whereas values close to one indicate well-resolved model parameters.

The choice of a survey layout, configuration type and selection of data governs the structure of the Jacobian $\boldsymbol{J}$, which is the foundation of the approximate Hessian matrix $\mathbf{H} = \mathbf{J}^T\mathbf{J}$. The reliability of the model update depends primarily on our ability to invert the matrix $(\mathbf{J}^T\mathbf{J} + \mathbf{C}_m^{-1})$. Without the regularization (damping and smoothing) this matrix would likely be singular. The eigenvalue spectrum of the approximate Hessian matrix is related to the null space or unresolvable model space of a particular data set. This allows comparison of spectra from various experimental designs as a quantitative method to rate specific information content, resolving ability and goodness of an experiment.

3. SYNTHETIC INVERSION EXPERIMENT METHODOLOGY

3.1 Experimental setup

The focus of the experiments was to determine the effect of the actual assumptions (anisotropy or isotropy) used in the forward solver and sensitivity calculations for the same inversion routine on a number of different anisotropic models. Therefore, most experiments were conducted with a three-sided geometry (combined cross-hole and borehole-to-surface) chosen because it delivered the most optimal possibility for data collection and model coverage. Such configurations are becoming more popular in field surveying. This type of electrode placement allows one to overcome the ambiguity from the principle of equivalence (Keller & Frischknecht 1966) associated with pure surface measurements when the axis of symmetry is vertical.

The experimental setup consisted of 78 electrodes, 32 in each borehole and the remaining 14 positioned along the surface. The positions of electrodes are shown by triangles in Fig. 2. Electrodes are placed at 5 m spacing. The two boreholes extend to a depth of 155 m and are spaced 75 m apart.

3.2 Forward and inverse parametrization

The model domain was discretized for inversion with a regular grid of rectangular model cells of size 5 m × 5 m. Inversion cell size was chosen to be the electrode spacing so as to limit the total number of model parameters because of the already increased number of parameters which must be considered when anisotropy is incorporated. There were 465 (31 × 15) inversion model cells for each parameter. The forward modelling was conducted with the same subdomain parametrization as the inversion cells. The forward calculation used a Gaussian nodal order of five for each subdomain along with 20 wavenumbers. This gave rise to 6897 nodes in the forward GQG grid ($[(N_{X1}-1).(N_{\text{ord}}-1)+1]\,.\,[(N_{Z1}-1).(N_{\text{ord}}-1)+1]$ where $N_{X1} = 31$, $N_{Z1} = 15$, $N_{\text{ord}} = 5$). This was deemed to be a good compromise between accuracy and computational efficiency (Greenhalgh 2008; Zhou *et al.* 2009).

To provide a comparison with the optimal three-sided cross-hole experiment, and to show what is possible with surface measurements alone in the presence of anisotropy, a surface electrode array numerical experiment was also conducted. Sixty-one electrodes were placed along the surface at a spacing of 5 m. The model (inner) domain extended from $x = 0$ to 300 m and in depth to $z = 60$ m. The same forward and inversion discretization was used as in the three sided experiments, that is 720 inversion cells of size 5 m × 5 m with 720 forward subdomains and 10 845 Gaussian nodes (Gaussian nodal order of 5).

3.3 Electrode array types

The three most widely used measurement configurations in cross-hole or surface-to-borehole geo-electric surveying are the pole–pole, pole–dipole and dipole–dipole arrays involving 2, 3 and 4 mobile electrodes, respectively. For pole–dipole and pole–pole the remote electrodes are located at a considerable distance away from the survey area so that there is no effective contribution from the current sink. This section of the paper explains the basis and selection for the comprehensive data sets used. Secondly, we explain a method for selection of the highest sensitivity data sets obtained from calculation of the Jacobian for comprehensive data sets.

A comprehensive data set (Xu & Noel 1993) consists of every possible non-reciprocal measurement, whereas a complete data set is composed of all linearly independent measurements. It is possible to reconstruct the comprehensive data set from the complete set (Lehmann 1995; Blome 2009). The pole–pole comprehensive and complete data sets are equivalent and consist of 3003 recording configurations (78 × 77 / 2) for a 78 electrode surface to cross-hole experiment.

Zhou & Greenhalgh (2000) conducted a thorough investigation into the sensitivity of various cross-hole electrode configurations, finding that sensitivity was improved along the midpoint region of the boreholes for configurations such as the bipole–bipole AM–BN in which current source (A) and sinks (B) and potential electrodes (M, N) are in different boreholes, that is borehole 1: A, M; borehole 2: B, N. This array also produces relatively large signals. Pole–dipole arrays were found to produce good results, however configurations such as A-MN and MN-A are susceptible to noise due to low voltage drop readings. The same is true for the 4-point configuration AB-MN and even though it offers improved resolution, it is at the expense of noise capture, especially due to the borehole fluid effect as recently investigated by Doetch *et al.* (2010).

It has been commonplace for some time with other geophysical techniques (e.g. seismic) to collect vast data sets. In geoelectrics

it only became feasible in recent times to record massive data sets efficiently; currently a 64 channel resistivity system exists having capacity to collect such sets (Zhe *et al.* 2007), and a 120 channel parallel recording system has recently been described by Blome *et al.* (2011). This, combined with advances in computer memory and parallel processing techniques, could make inversion with comprehensive data sets possible in the future. However currently the massive amount of data involved in comprehensive pole–dipole and dipole–dipole data sets for even 78 electrodes is usually prohibitive for inversion because of time and computer memory constraints. To reduce the computational burden, it is normal practice to discard data points corresponding to high geometric factors K, which often correspond to low signal levels and therefore likely to be contaminated by noise. To illustrate the point, by eliminating all data having geometric factors $K > 500$ m, a comprehensive pole–dipole data set of 78 electrodes still has ∼76 000 data. This is still a large amount of data to invert. For the same number of electrodes but in a 4-point comprehensive AM–BN (bipole–bipole) configuration, eliminating data with $K > 500$ m) results in a set of >500 000 data points.

3.4 Selecting the high sensitivity configurations

From examination of the Jacobian matrix for the comprehensive data sets, there exists a large subset of data that has extremely small sensitivity magnitude. The motivation of saving computer memory and run time resources directs us to investigate the effect of discarding low sensitivity data from comprehensive data sets and working with a reduced (filtered or selected) version. Such an approach was recently advocated by Athanasiou *et al.* (2009). In earlier optimized experimental design strategies described by Stummer *et al.* (2002) and Wilkinson *et al.* (2006), configurations were progressively selected in accordance with linear independence or contributing most towards improving model resolution. The latter approach entails having to sequentially compute the model resolution matrix for each electrode configuration added to the set, and is very computationally intensive. By contrast, our sensitivity selection strategy is far less demanding than that based on incremental improvements to resolution, and seems adequate for the purpose.

An initial choice must be made for the model used to calculate the Jacobian. This is an arbitrary choice and may include any *a priori* knowledge. We chose an isotropic model having $\rho_L = \rho_T = 500$ Ohm m because this is the starting model given for our inversions.

The method of filtering (or selecting entries from) the Jacobian was, first, to split the matrix into separate model parameters: ρ_L and ρ_T. The separate matrices (of dimension number of electrode configurations times the number of model cells) were then sorted along the model cell column in order of increasing sensitivity magnitude. Data may then be selected from each model cell column subject to either the absolute magnitude of the sensitivity or the number of data to include per model cell. Non-unique (dependent) data points are eliminated. A secondary beneficial outcome of the filtering process originates from prior knowledge of resolution patterns. Regions of low resolution model cells such as at the centre section of the boreholes can be allotted increasing numbers of selected high magnitude sensitivity data. The data inclusion method we used for our selected (filtered) data set was to take progressively increasing amounts of data for model cell columns as one moved from the boreholes towards the central column of cells. This is illustrated diagrammatically in Fig. 4.

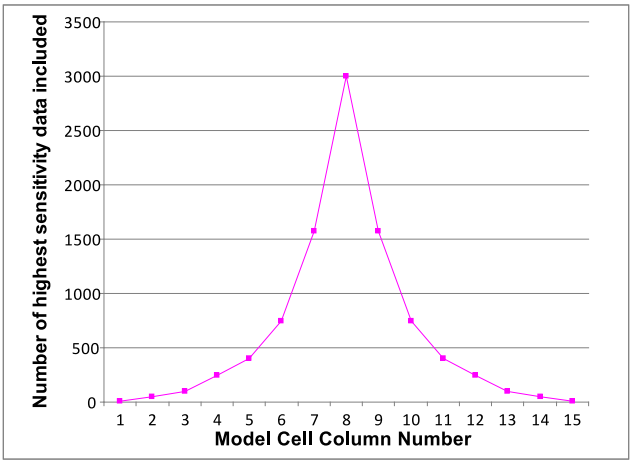

Figure 4. A representative graph of the data selection strategy that filters out ineffective low sensitivity data by sorting and selecting high sensitivity data. The *x*-axis represents the model cell column number (numbers 1 and 15 define the edge of the model/borehole). Increasing amounts of data are included towards the model cell column 8 which represents the lowest resolution along the central axis between the boreholes.

With the filtering/selection strategy used, the comprehensive pole–dipole data set of 77 000 pole-measurements is reduced to 8036 data points. The corresponding dipole–dipole comprehensive set of 549 000 configurations is reduced to 159 000 data points

3.4 Types of models

Three types of anisotropic model were investigated: first, an anisotropic background (TTI) having an embedded isotropic block anomaly. This type of model could simulate the geological situation of tilted shale or fractured limestone as the background rock, and an igneous inclusion or a pure water or air filled cavity causing the high resistivity anomaly. The second type of model is the reverse of the first type, involving an isotropic background with an anisotropic inclusion. This type of model could be representative of sandstone with enclosed clay or jointed ore body inclusion. The third model involves a layered anisotropic sequence that could simulate volcanic flows or metamorphic units of dissimilar dip.

The anisotropic model parameters allow for the possibility of changing the magnitude (coefficient) of anisotropy and/or the orientation of the axis of symmetry.

4 RESULTS

4.1 Anisotropic background with an isotropic block inclusion

The models used to create the synthetic data sets in this section consisted of an anisotropic background with a rectangular high resistivity isotropic target (1250 Ω m) centred between the boreholes. This section of the paper focuses on the effects of inversion reconstructions for variations in the orientation of the plane of isotropy (i.e. the θ_0 angle) and the strength (coefficient) of anisotropy (λ).

For this preliminary experiment the comprehensive pole–pole data set (3003 data points) was employed for two reasons. First, this basis of measurements contains all possible linearly independent subsurface information, and secondly, the relatively small data set minimized the computational time required.

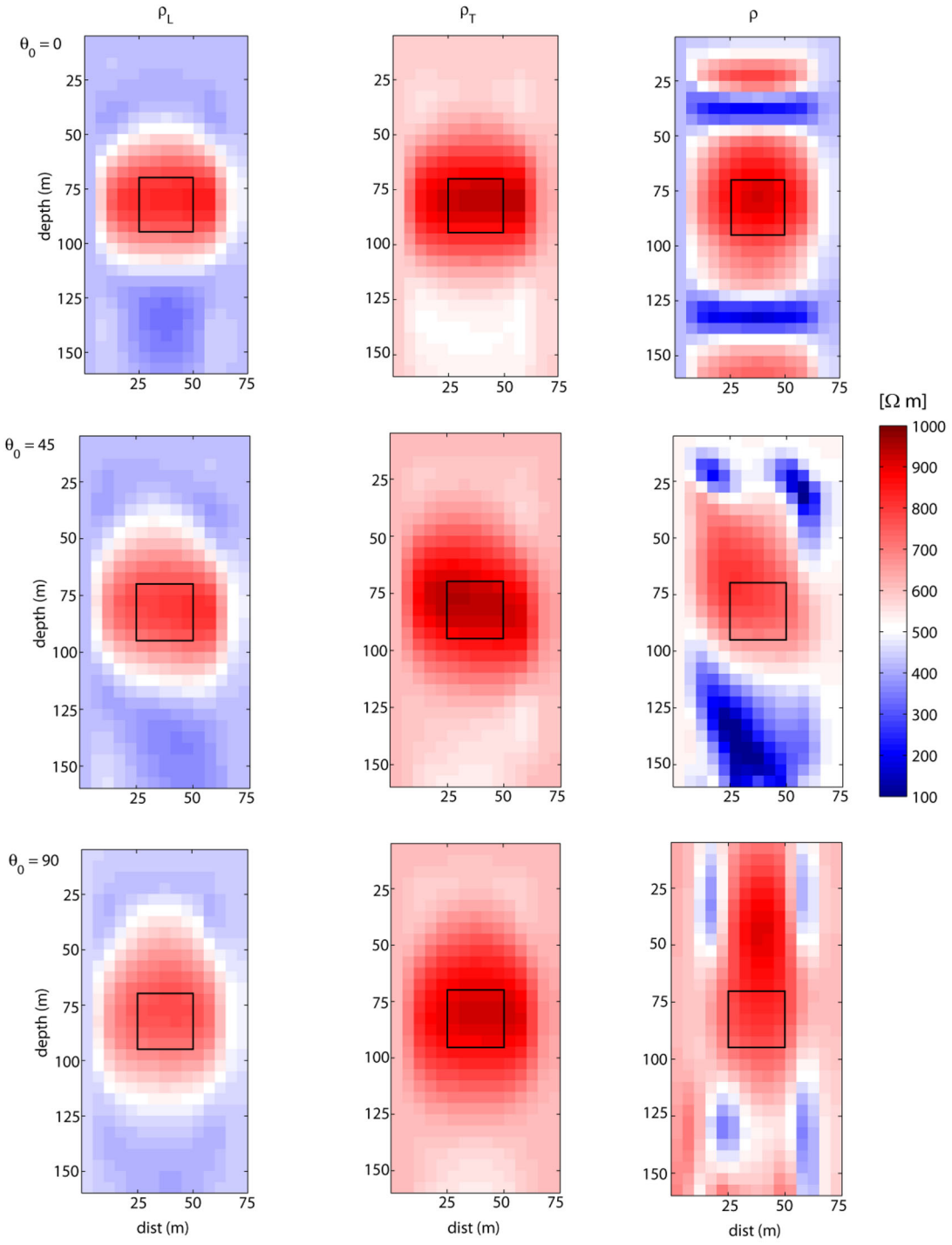

Figure 5. The comprehensive pole–pole data set inversion reconstruction of an anisotropic background model (constant $\lambda = 1.22$) with isotropic inclusion (1250 Ohm m). The left-hand (ρ_L) and middle (ρ_T) columns are produced with the anisotropic assumption while the right-hand column assumes isotropy (ρ). The axis of symmetry (normal to plane of isotropy) varies from $\theta_0 = 0°, 45°, 90°$ in the top, middle and bottom rows, respectively.

Fig. 5 exhibits the inversion results for a set of true models in which the axis of symmetry angle θ_0 has three distinct values of 0, 45° and 90°, as shown in the top, middle and bottom rows, respectively. This is physically equivalent to the orientation of the plane of isotropy (stratification or foliation) being horizontal, dipping and vertical. The coefficient of anisotropy is fixed at $\lambda = 1.22$ ($\rho_L = 400\,\Omega\,m$, $\rho_T = 600\,\Omega\,m$). The starting resistivity given for the inversion was a homogeneous and isotropic model having $\rho_L = \rho_T = 490\,\Omega\,m$, which is equal to the geometric mean resistivity ρ_m. The isotropic nature of the starting model ensured that the anisotropic and isotropic assumption-based inversions could be made as nearly equivalent as possible, at least from the initial model viewpoint.

The left-hand and middle columns of Fig. 5 represent the inversion results (damping factor of 0.000005) after 20 iterations for ρ_L and ρ_T produced with the correct anisotropic assumption

for forward modelling and sensitivity calculations. Note that only the parameters ρ_L and ρ_T are inverted for, with θ_0 held fixed. The right-hand column gives the corresponding inversion result for the scalar resistivity ρ produced with the widely used isotropic assumption. The ρ_L and ρ_T images show accurate reconstruction of the anisotropic nature of the true background resistivity for all angles of the plane of isotropy. It can be seen that for all θ_0 values the positions of the true high resistivity isotropic embedded anomaly (outlined by the black square) are well resolved for both ρ_L and ρ_T images. An underestimate of the true high resistivity anomaly is notable in the ρ_L image; however, the contrast between the background and the reconstructed anomaly is equal to that of the ρ_T images. The reconstructed target anomalies were somewhat smeared over the borders of the true known geometry, although importantly they were centred in the correct position. This smearing is a product of the inversion scheme which we made with basic functionality. More complicated inversion objective functions (e.g. L1 norm, different smoothing in horizontal and vertical directions, penalty terms for anisotropy) exist that could likely improve the results (see Pain *et al.* 2003; Greenhalgh *et al.* 2006), however these were not included so as to not deflect from the main objectives of the experiment, which was to compare inversion of anisotropic data using both anisotropic and isotropic algorithms.

The images obtained with the incorrect isotropic assumption (right-hand column Fig. 5) after 20 iterations (damping factor 0.000001) show a notable banding effect which follows a parallel orientation to the plane of isotropy for each of the different values (0°, 45° and 90°). The data misfits obtained by the set of inversions using the isotropic assumption were more than eight times higher than those produced with the anisotropic assumption, which were deemed to be within the numerical noise level (1–2 per cent). The anisotropic inversion data rms values lie in the range 1.66–1.92 whereas the isotropic inversion values range from 15.6 to 20.3. The corresponding model rms error values vary from 0.016 to 0.050 (anisotropic inversion) to 20.7–21.9 (isotropic inversion). The higher rms values and the banded artefacts both result from the inability of the isotropic inversion to fit the data derived from an anisotropic synthetic model. The source of the banding is the difference of sign in regions of the subsurface for isotropic Fréchet derivatives in anisotropic media. This has been described in Wiese *et al.* (2009) and quantified in Greenhalgh *et al.* (2010).

We now present in Fig. 6 the effects of the magnitude of anisotropy of the background medium for the same style of model as above. Anisotropy was varied from slight (almost isotropic) values to highly anisotropic values, where conductivity was four times larger parallel to the plane of isotropy than perpendicular to it. The true models used had $\theta_0 = 45°$, with the coefficient of anisotropy varied from $\lambda = 1.05$ ($\rho_L = 475\,\Omega\,m$, $\rho_T = 525\,\Omega\,m$), $\lambda = 1.5$ ($\rho_L = 300\,\Omega\,m$, $\rho_T = 700\,\Omega\,m$) and $\lambda = 2$ ($\rho_L = 200\,\Omega\,m$, $\rho_T = 800\,\Omega\,m$) in the top, middle and bottom rows, respectively. The isotropic anomaly resistivity value is 1250 Ω m. The inversion results presented in Fig. 6 are in the same format as in Fig. 5, that is, ρ_L and ρ_T in the left-hand and middle columns with ρ in the right-hand column. The starting model used for the inversions was again the homogeneous isotropic resistivity equal to the geometric mean of the true anisotropic values of the background. All involved a damping factor of 0.000005 and the number of iterations varied from 6 to 20.

The reconstructions performed under the anisotropic assumption are accurate in resolving the true background resistivities. The rms model error values are in the range 0.022 ($\lambda = 1.05$) to 0.177 ($\lambda = 2$). The corresponding data misfit rms values vary from 1.35 to 1.95. The increasing anisotropy (i.e. difference between ρ_L and ρ_T) is especially apparent by the intensifying colour values (both red and blue) from the top to bottom rows of the figure. The high resistivity anomaly is centred over the true position (outlined in black) for all coefficients of anisotropy. However, the reconstructed anomaly in the ρ_L image decreases in resistivity with increasing λ, whereas the opposite trend occurs for ρ_T. The ratio between the background and the anomaly resistivity is comparable for both ρ_L and ρ_T resistivities for the intermediate and high λ values. The effect of the angle of the symmetry axis ($\theta_0 = 45°$) is apparent, since the reconstructions undertaken with the incorrect isotropic assumption show the target to be elongated along this orientation for large anisotropy coefficient values. The high resistivity target was harder to image for the high λ value (bottom row) because the ρ_T background increased to such an extent that the difference between the background resistivity and that of the anomaly became much less significant.

The image obtained using an isotropic inversion algorithm shows superior recovery of the isotropic block for slight anisotropy (top row) to that obtained with an anisotropic inversion, specifically in terms of the resistivity structure resolved compared to the true model. However, for increasing coefficients of anisotropy (middle and bottom rows), spurious low resistivity artefacts become apparent. A region of high resistivity is resolved but it is greatly stretched in the direction parallel to the plane of isotropy. The banded artefacts also parallel this orientation. The data misfits for these inversions increased with the coefficient of anisotropy from 0.99 to 14.9 (>7 times the numerical noise), apart from the almost isotropic model in which the isotropic inversion converged to the numerical noise levels of 1–2 per cent. All the inversions undertaken with the correct anisotropic assumption converged to within numerical noise levels of 1–2 per cent. The model rms error values for the isotropic inversions range from 127 ($\lambda = 1.5$) to 153 ($\lambda = 2$), which are very much larger than the corresponding anisotropic inversions.

We next investigate a similar type of anisotropic background model but this time with two embedded isotropic targets, one high resistivity (1250 Ωm), the other low resistivity (50 Ωm), and using a purely surface electrode array involving 61 electrodes. The pole–dipole comprehensive set (but with large geometry factor ($K > 500$ m) data filtered out) of 12 511 electrode configurations was employed for the reconstruction. The true models used had an axis of symmetry of $\theta_0 = 45°$, with the coefficient of anisotropy for the background varied from $\lambda = 1.1$ ($\rho_L = 450\,\Omega m$, $\rho_T = 550\,\Omega\,m$), $\lambda = 1.4$ ($\rho_L = 325\,\Omega\,m$, $\rho_T = 675\,\Omega\,m$) and $\lambda = 2$ ($\rho_L = 200\,\Omega\,m$, $\rho_T = 800\,\Omega\,m$), corresponding to the top, middle and bottom rows of Fig. 7, respectively. The inversion results are given in the same format as before, with the reconstructed ρ_L and ρ_T values shown in the left-hand and middle columns of Fig. 7, and the isotropic inversion result for ρ given in the right-hand column. Inversions were again started with isotropic resistivities equal to the geometric mean of the true values. A damping factor of 0.00005 was used and the number of iterations varied from 8 to 17.

The reconstructions carried out with the anisotropic assumption are accurate (model rms error values in the range 0.04–0.31, corresponding data rms values in the range 0.60–1.9), and able to resolve the increasing anisotropy which is apparent from the changing colours from the top to bottom rows. Both high and low resistivity anomalies are centred over their true positions (outlined in black) for all magnitudes of anisotropy. However, the reconstructed high resistivity target in the ρ_L image decreases in resistivity magnitude notably at $\lambda = 2$. In the ρ_T images, the high resistivity target becomes poorly resolved as λ increases. The resolving power of the

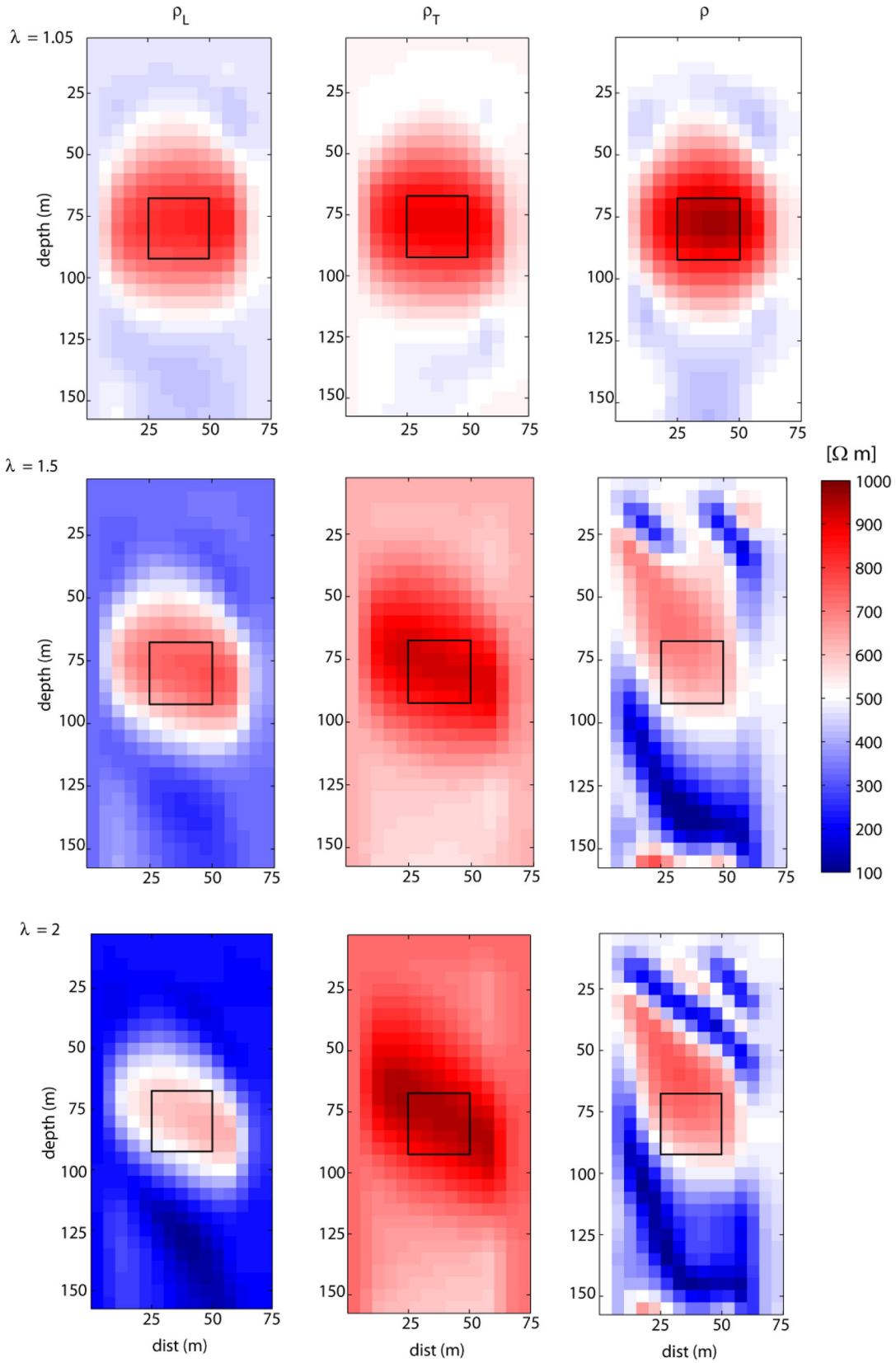

Figure 6. The comprehensive pole–pole data set reconstruction of anisotropic background model ($\theta_0 = 45°$) with isotropic inclusion (1250 Ohm m). The true model magnitude of anisotropy varies $\lambda = 1.05, 1.5, 2$ from top to bottom rows. The columns are in the same format as Fig. 5.

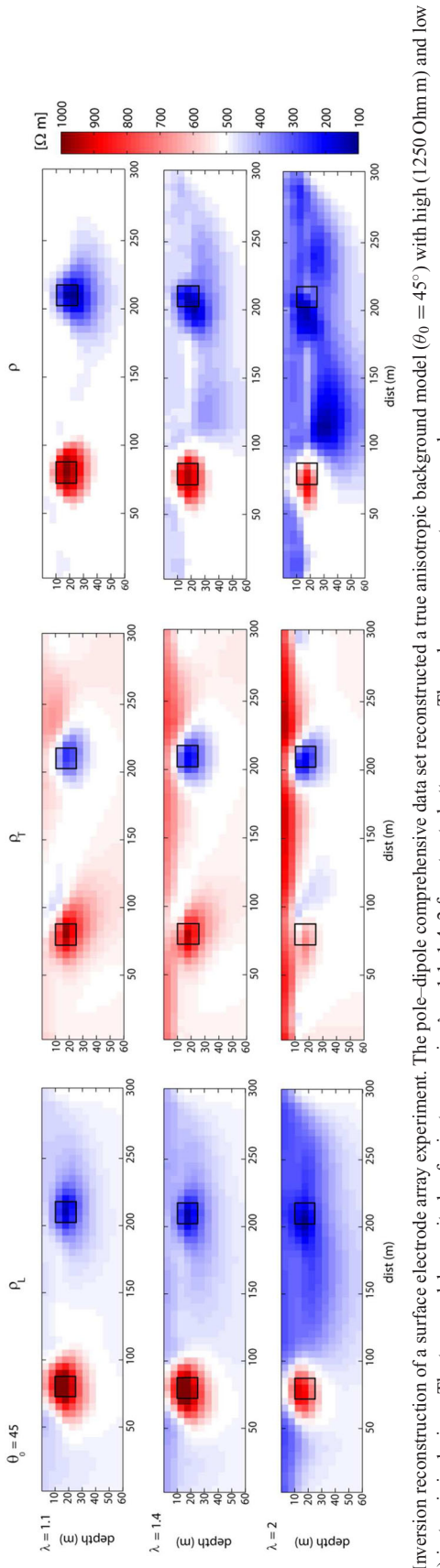

Figure 7. Inversion reconstruction of a surface electrode array experiment. The pole–dipole comprehensive data set reconstructed a true anisotropic background model ($\theta_0 = 45^\circ$) with high (1250 Ohm m) and low (50 Ohm m) isotropic inclusions. The true model magnitude of anisotropy varies $\lambda = 1.1, 1.4, 2$ from top to bottom rows. The columns represent ρ_L, ρ_T and ρ.

ρ_T parameter drops with depth far more significantly than ρ_L (see Wiese *et al.* 2009).

The image obtained with the incorrect isotropic assumption (isotropic inversion code) shows superior recovery of the isotropic blocks for the slight anisotropy case (top row) compared to that using an anisotropic inversion, specifically in terms of the level of target resistivity resolved (although the overall model rms error is higher at 2.59; the rms data misfit is also higher at 1.56). However, for the model with a high level of anisotropy (bottom row), spurious low resistivity artefacts become apparent in the isotropic image. The data misfits with the isotropic inversion (rms values 1.5–9.6) are not as high as in the three-sided experiments (Figs 5 and 6), but the same trend of increasing data rms with increasing levels of anisotropy is again observed. The corresponding model rms errors are 5.76 ($\lambda = 1.4$) and 6.67 ($\lambda = 2$), two orders of magnitude higher than for the anisotropic inversions.

4.2 Isotropic background with an anisotropic block inclusion

In this section, we present inversion results for an anisotropic target (block) in an isotropic background. The target is located midway between the boreholes and has square geometry; its electrical properties are $\rho_L = 250\,\Omega$ m, $\rho_T = 750\,\Omega$ m ($\lambda = 1.7$) with $\theta_0 = 45^\circ$. The isotropic background is $\rho_L = \rho_T = 500\,\Omega$ m. Inversion results from a range of different electrode configurations and data sets are presented and compared. All inversions were started with an isotropic assumption $\rho = \rho_L = \rho_T = 500\,\Omega$ m.

Fig. 8 shows the inversion results for the pole–pole comprehensive (top row), the pole–dipole selected (middle row) and pole–dipole comprehensive (bottom row) data sets. The left-hand and middle columns correspond to anisotropic reconstruction ρ_L and ρ_T and the right-hand column is the isotropic ρ. The damping factors were 0.000005 (anisotropic inversion) and 0.0005 (isotropic inversion). The number of iterations reached the maximum (20) for the anisotropic inversions but convergence was reached sooner (iterations 4–8) in the isotropic case.

The pole–pole anisotropic inversion updated the ρ_L and ρ_T model parameters in the correct direction (data rms of 1.91, model rms error of 0.0088), with the spatial reconstruction giving the target anomaly at the true position (outlined by the black square). Resolution is more limited towards the centre of the boreholes, especially for ρ_T. The corresponding isotropic inversion produced artificial banding which is oriented in a direction parallel to the plane of isotropy. The data misfit value of 10.82 is much higher, as is the model rms error of 4.92.

The pole–dipole comprehensive data, when inverted, resolved the anisotropic anomaly in terms of spatial sharpness and yielded resistivities closer to the true values than in the pole–pole case. It gave a slightly lower model rms error value of 0.0073 but comparable data rms of 1.92. Although the resistivity scale of the pole–dipole filtered data set inversion was slightly inferior to the comprehensive set, the reconstruction was very efficient by comparison, with similar results achieved using considerably less data and computer resources. The data rms was marginally higher at 1.98. The isotropic assumption inversions had data misfits more than ten times larger than the numerical noise limits inherent in the forward modelling scheme, and 5–10 times higher than for the anisotropic inversions. The cause of the large misfits is the trend of artificial banding patterns of alternating high and low resistivity that lie parallel to the orientation of the plane of isotropy. The model rms errors for the

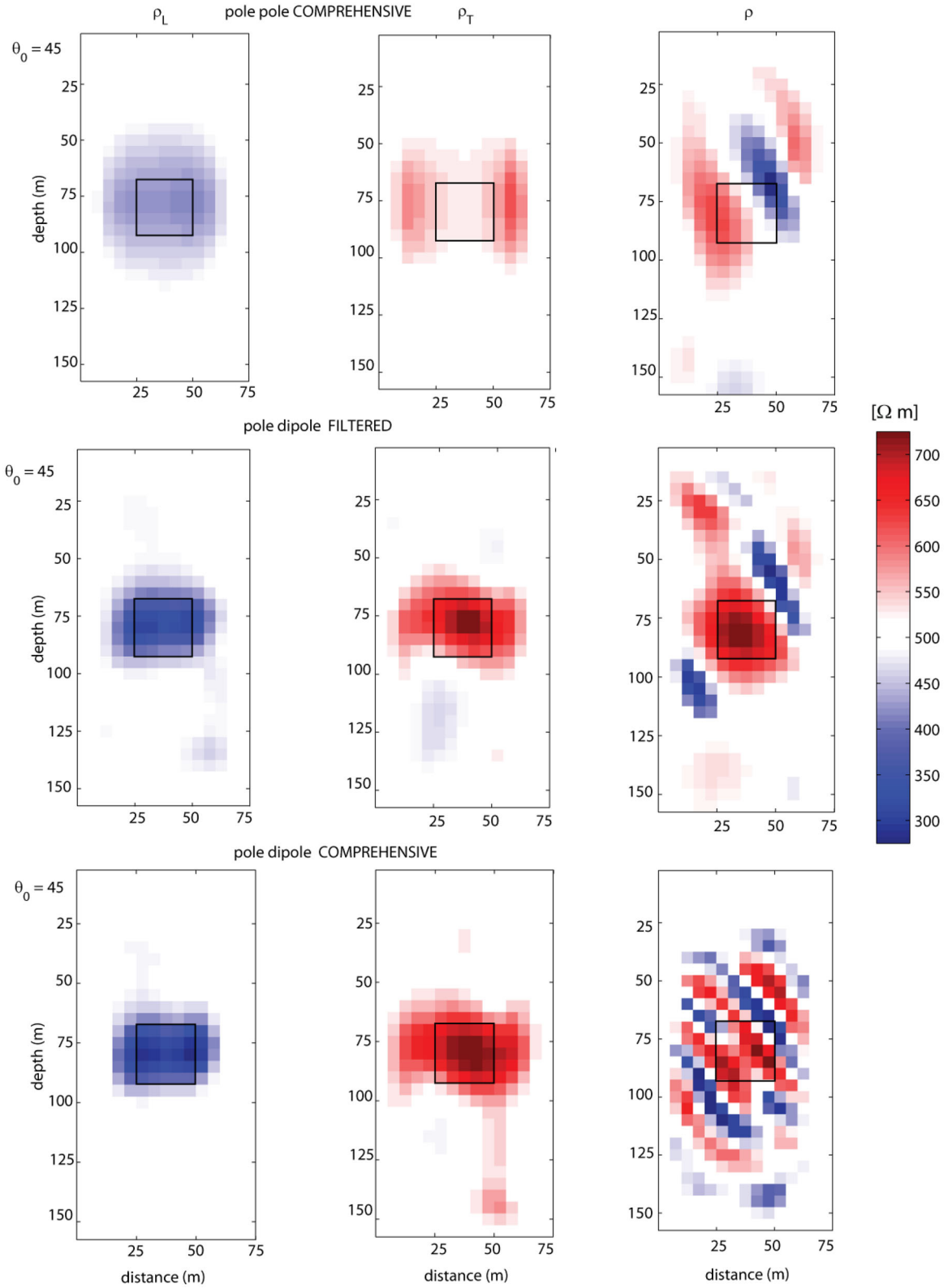

Figure 8. The pole–pole comprehensive (top), pole–dipole selected (middle) and pole dipole comprehensive (bottom row) inversion images for a model consisting of an isotropic background (500 Ohm m) with an anisotropic inclusion ($\lambda = 1.7$) and $\theta_0 = 45^\circ$.

isotropic case are in the range 4.9–9.5, very much larger than for the anisotropic inversions.

In Fig. 9, we show inversion results for the pole–dipole comprehensive data set using the same model as in Fig. 8, but the axis of symmetry of the target is varied through $\theta_0 = 0^\circ, 45^\circ, 90^\circ$ from the top to the bottom row. An alternative form of presentation is used for the anisotropic parameters this time, with ρ_m and λ shown in the left- and right-hand columns, respectively. The λ

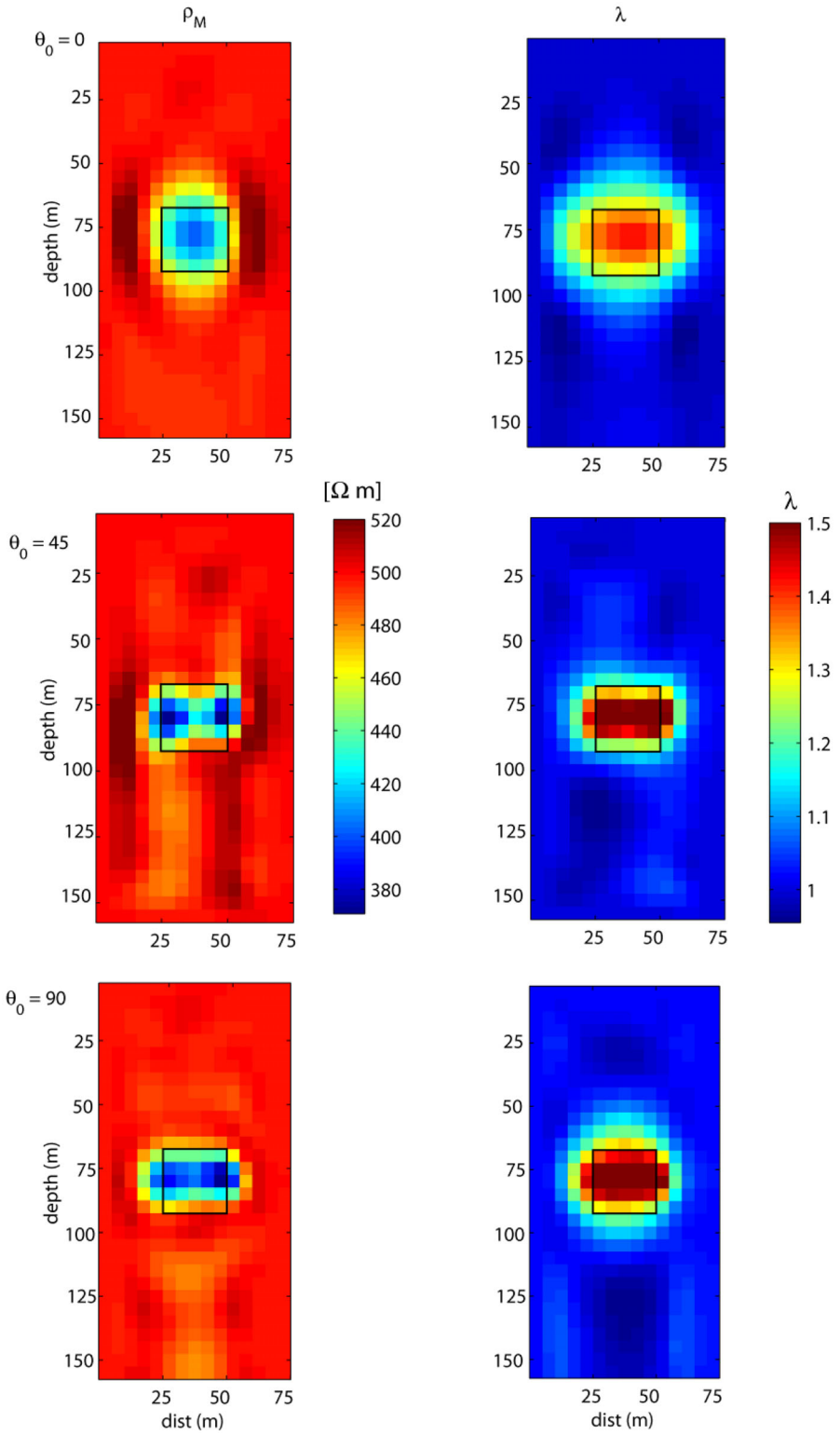

Figure 9. Alternative representation of the anisotropic model parameters produced by inversion using the pole–dipole comprehensive set. The mean resistivity (ρ_{m}) and the coefficient of anisotropy (λ) are displayed in the left-hand and right-hand columns, respectively. The true model is the same as Fig. 8 except the rows correspond to differing axis of symmetry angles: $\theta_0 = 0^\circ, 45^\circ, 90^\circ$ from top to bottom.

plot is particularly revealing, indicating the correct true isotropic background ($\lambda \approx 1$). The anisotropic anomaly region is accurately represented with reddish colours, slightly underestimating the true value of ($\lambda = 1.7$). Data rms values are all close to 1.9 and the model rms errors range from 0.0088 ($\theta_0 = 0^\circ$) to 0.054 ($\theta_0 = 90^\circ$). The ρ_{m} images are hard to use for direct interpretation because it is a derived rather than physical quantity, and the anomaly region is dominated by the lower resistivity of ρ_{L} and ρ_{m}. This type of

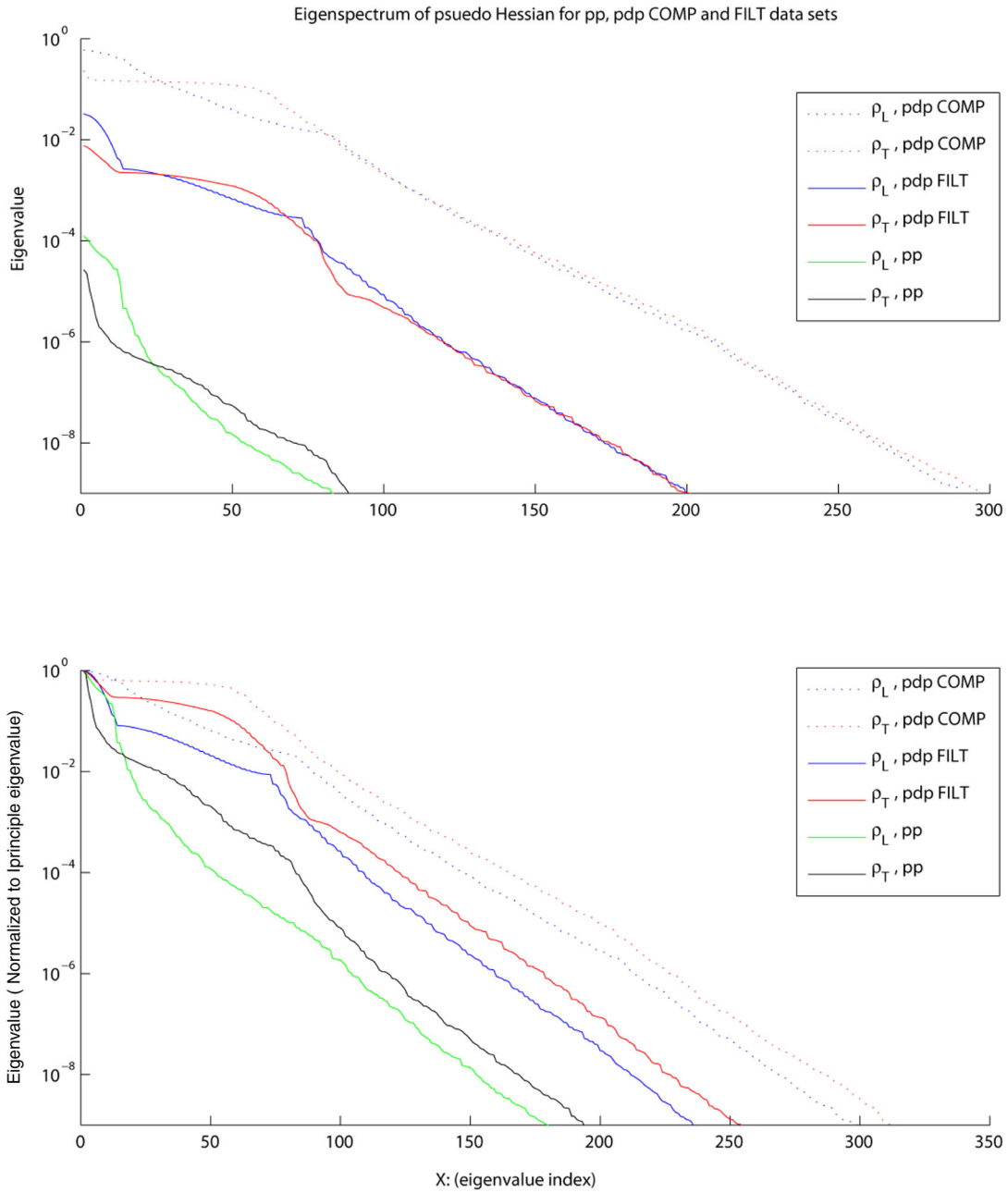

Figure 10. Raw (top panel) and normalized (bottom panel) eigenspectra of the pseudo-Hessian matrix ($J^T J$) for the pole–pole comprehensive (pp), pole–dipole selected (pdp SELECT) and pole–dipole comprehensive (pdp COMP) data sets. The calculation was based on the same model as in Fig. 8.

representation nevertheless has interpretative value, as demonstrated in Kim *et al.* (2006), who were able to successfully delineate cavities by identifying regions of isotropy amongst an anisotropic background. The isotropic regions were cavities filled with either water or air.

To further quantify the goodness of the different data sets, we show in Fig. 10 the normalized eigenvalue spectra calculated based on the true model (i.e. $\rho_{\mathrm{L}} = 250\,\Omega\,\mathrm{m}$, $\rho_{\mathrm{T}} = 750\,\Omega\,\mathrm{m}$ (i.e., $\lambda = 1.7$) with $\theta_0 = 45^\circ$) First, it is notable that the spectra for ρ_{L} and ρ_{T} generally follow the same pattern except for low indices for the pole–pole data set. There is a distinct difference between the pole–pole and pole–dipole dominant eigenvalues, with the pole–dipole sets being larger by more than five orders of magnitude. The pole–dipole filtered and comprehensive sets are indistinguishable until approximately the 75th eigenvalue, where the comprehensive set assumes a gentler slope. The slopes of the spectra from the 200th eigenvalue onwards are close to parallel but the pole–dipole comprehensive curve is offset two orders of magnitude higher than the pole–pole data set and has the smallest null space of the three sets. Here the null space can be thought of as the unresolvable model parameters and therefore gives a good comparison between information content of the different data sets.

Fig. 11 displays the diagonal elements of the formal model resolution matrix, R_{ii} (see eq. 19) plotted at the respective model cells. The model used for this calculation was the anisotropic block model used throughout this section. The left-hand columns of Fig. 11

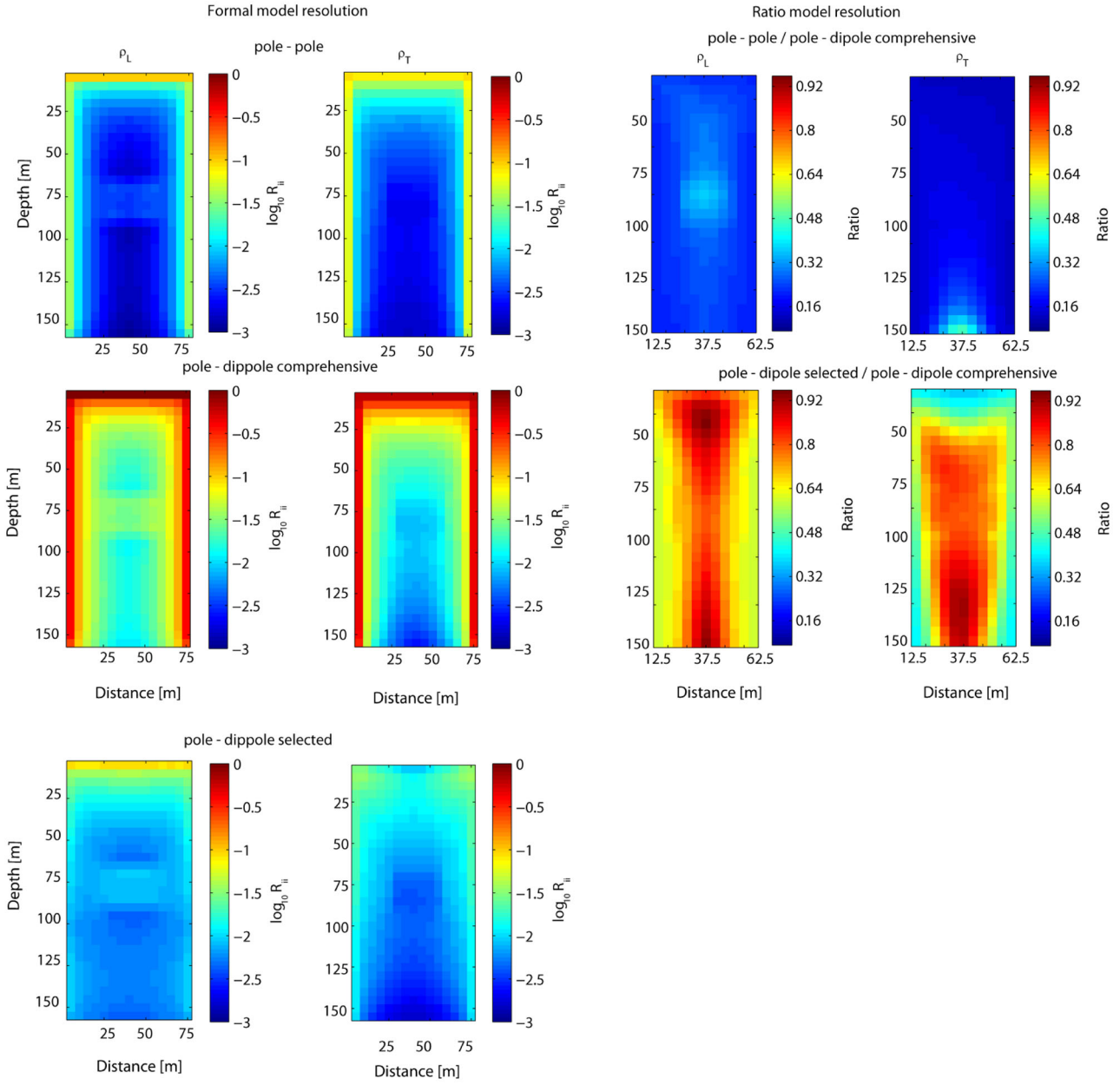

Figure 11. The formal model resolution (R_{ii}) is displayed in the two left-most columns for the pole–pole (top row), pole–dipole comprehensive (middle row) and selective pole–dipole data sets (bottom row). The calculation was based on the same model as in Fig. 8. The two right-most columns display the ratio of the formal model resolution for the pole–pole (top row) and the pole–dipole selective (bottom row) with respect to the optimal pole–dipole comprehensive resolution.

display the resolution for pole–pole (top) and pole–dipole comprehensive (middle) and the pole–dipole selective data sets for both ρ_L and ρ_T model parameters. For both ρ_L and ρ_T parameters the highest resolution is seen closest to the electrodes for all data sets. The difference in resolution values between ρ_L and ρ_T is due to the difference in sensitivity patterns, which is documented in Wiese *et al.* (2009). In general, parameter ρ_L exhibits superior resolution at the centre of the model than does ρ_T.

A direct comparison of the resolving power for each data set is presented in the right-hand columns of Fig. 11. The top panel shows the model resolution ratio of the pole–pole with respect to the pole–dipole comprehensive set, the bottom panel shows the pole–dipole selected data set with respect to the pole–dipole comprehensive set. The top ratio plot clearly show the superiority of the pole–dipole comprehensive set over the pole–pole set, with ratios below 20 per cent in the majority of model cells. The selective (filtered) pole–dipole set shows high ratios greater than 70 per cent of the pole–dipole comprehensive set for the central model region, which illustrates the merits of selecting data based on sensitivity considerations.

4.3. Three parameter inversion

In the previous sections we focused on resistivity inversion incorporating anisotropy, and the erroneous results obtained using an

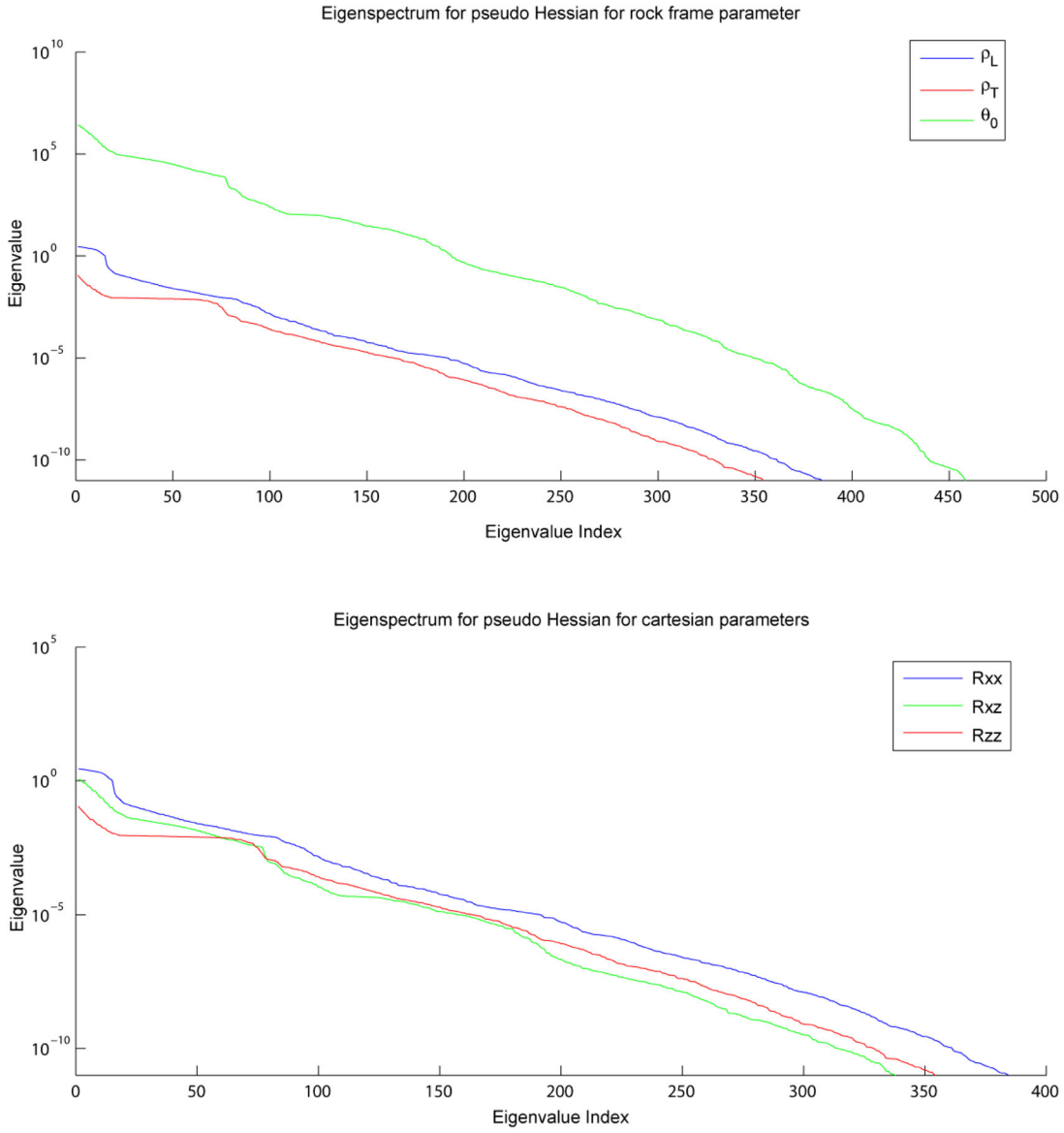

Figure 12. Three parameter eigenspectra comparison between eigen (or rock) frame (top panel) and Cartesian (bottom panel) parameters for an anisotropic block model with $\lambda = 1.4$ and $\theta_0 = 45^\circ$. Note the orders of magnitude difference between the eigenframe parameters, whereas the Cartesian parameters are all of similar order.

incorrect isotropic inversion scheme. The anisotropic inversions were established for the two parameters ρ_{L} and ρ_{T}, with a fixed but arbitrary angle defining the orientation of the symmetry axis. This method of constraint, by decreasing the number of model parameters to be solved for, effectively stabilizes the inversion without specifically penalizing anisotropy. In this section we broaden the inversion to obtain all three parameters at each cell for a 2-D TTI model. Previous studies (e.g. Herwanger *et al.* 2004; LaBreque *et al.* 2004; Kim *et al.* 2006; Yi *et al.* 2011) have all ignored the angle of anisotropy by assuming the principal resistivitiy directions coincide with the co-ordinate frame. The implication of including the extra model parameter (the orientation of the axis of symmetry) is to increase the non-uniqueness and non-linearity of the inversion problem. In Section 2.1, two equivalent descriptions for the three anisotropic model parameters were given, the Cartesian and the principal axis (eigen) frame.

As an instructive preliminary investigation to assess the preferred model description to use in the inversion, we computed the eigenvalue spectra of the pseudo-Hessian matrix for the two different formulations: ρ_{L}, ρ_{T}, θ_0 and ρ_{XX}, ρ_{XZ}, ρ_{ZZ}. These are shown in the top and bottom panels, respectively, of Fig. 12. The eigenspectra were calculated for a homogeneous anisotropic model with $\lambda = 1.4$ and $\theta_0 = 45^\circ$. The spectra are extremely similar, with the exception of the newly introduced parameters: θ_0, ρ_{XZ}. The spectra related to θ_0 are five orders of magnitude higher than ρ_{L}, ρ_{T} and the Cartesian parameters ρ_{XX}, ρ_{XZ} and ρ_{ZZ}. The sensitivities for the θ_0 angle are also orders of magnitude larger than the anisotropic resistivity model parameters. The source of the amplitude difference in the sensitivity and the eigenvalues most probably stems from the different units of the eigenframe model parameters θ_0 ($^\circ$) versus ρ_{L}, ρ_{T} (Ω m). Such large differences in sensitivity magnitude can destabilize an inversion (see later). This difference is not encountered in

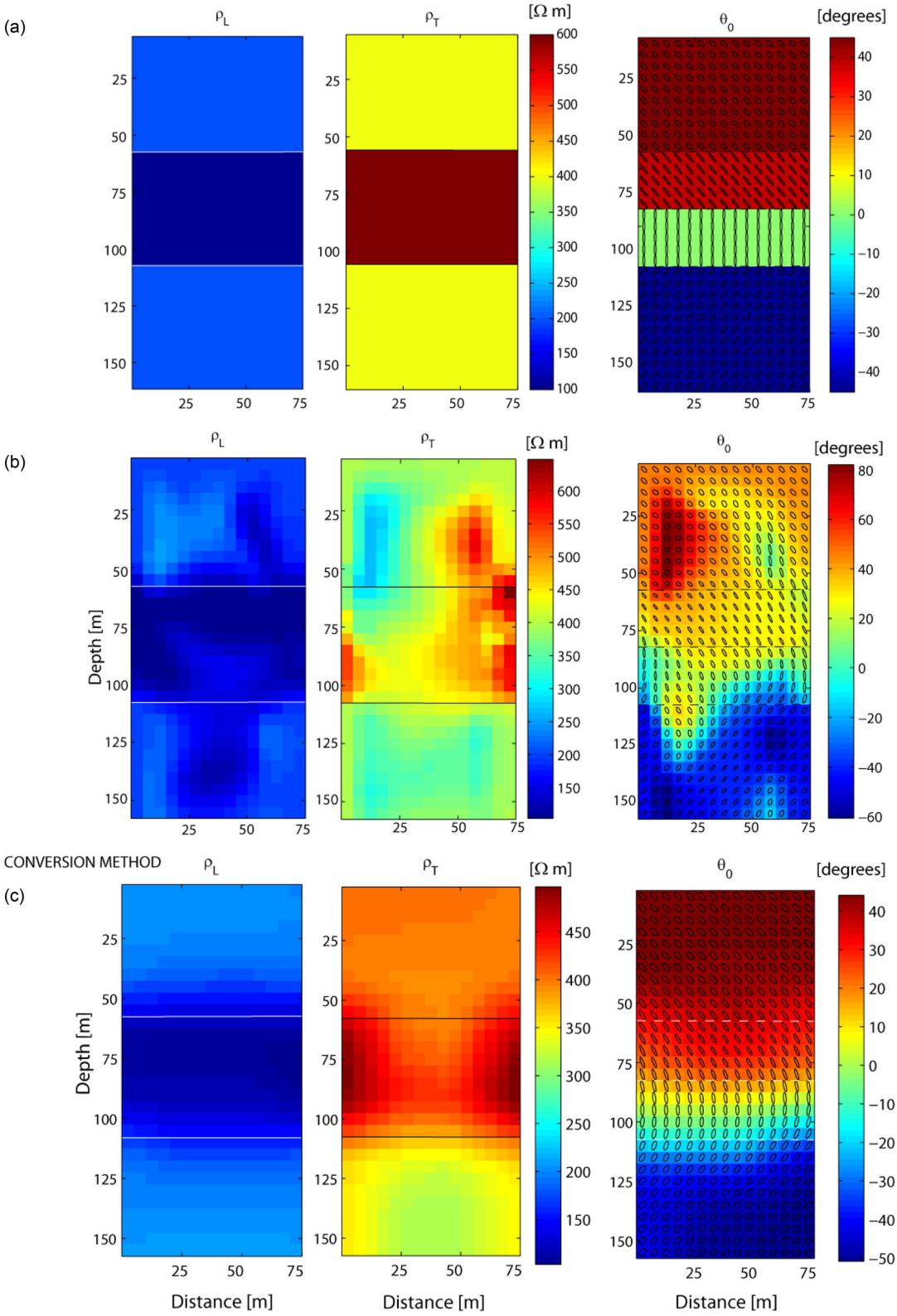

Figure 13. Three parameter inversion for a layered TTI media: (a) the true four layered synthetic model, (b) inversion result conducted in the eigen (or rock) frame, (c) inversion result conducted in the Cartesian co-ordinate frame and converted for presentation.

the Cartesian frame, because all parameters have similar sensitivity magnitude. However, the ρ_{xz} parameter is less intuitively meaningful than the θ_0 angle (which has its physical meaning described in the Background Theory section).

The ρ_L, ρ_T, θ_0 model employed to produce the first set of synthetic data for the three parameter inversion experiment is shown in Fig. 13(a). The model is a four-layered TTI medium, where each layer has a different coefficient of anisotropy and axis of symmetry

(or dip of the plane of isotropy). The ρ_L, ρ_T (or alternatively: ρ_{XX}, ρ_{ZZ}) parameters control the degree of anisotropy, which for this experiment is $\lambda = 1.4$ in the top and bottom layers and $\lambda = 2.4$ in the middle layer. The θ_0 parameters control the orientation of the TTI axis of symmetry, which varies in the four layers (from the top to bottom layer the values are $\theta_0 = 45, 37.5, 0, -45^\circ$, respectively).

Inversions of synthetic data from the same model were carried out using two different approaches. First, the natural rock frame model parameters were used directly. Secondly, the values were initially converted into the Cartesian domain values with forward calculations, sensitivity calculations and inversion model updates made with respect to the Cartesian model parameters. On completion of the inversion procedure, the Cartesian output values for the final images were transformed back into the ρ_L, ρ_T, θ_0 parameter form for display. An equivalent slightly anisotropic starting model was given for both inversions (e.g. $\rho_L = 260\,\Omega$ m and $\rho_T = 300\,\Omega$ m, $\theta_0 = 0^\circ$). Larger smoothing parameters were applied to both inversions to counteract the increased non-uniqueness of the inverse problem.

One attraction of working with the Cartesian frame is that all three parameters have the same units and comparable sensitivities. This is not the case for the eigenframe, because the dip angle parameter has different dimensions and far greater sensitivity values, as mentioned above. The effects of this will be evident later.

Fig. 13(b) shows the inversion results for the pole–dipole comprehensive data set carried out in the ρ_L, ρ_T, θ_0 domain, whereas Fig. 13(c) displays the corresponding results for the inversion performed in the ρ_{XX}, ρ_{XZ}, ρ_{ZZ} domain then converted to ρ_L, ρ_T, θ_0 for presentation. Both inversions involved damping factors of 0.00005 but the natural rock frame inversion involved fewer iterations (7) than for the Cartesian frame inversion (ITS = 18). Visual comparison of the reconstructions shows superior results for the inversion carried out in the Cartesian domain, although both yielded almost the same model rms error of 0.24. However the data rms for the Cartesian frame was just 2.25, almost a factor of 6 smaller than for the natural rock frame inversion. The Cartesian frame inversion was successful in delineating all layer boundaries and resolving the correct orientations of the resistivity ellipses of the true model. The large difference in magnitude of sensitivity between the model parameters destabilizes the linearized inversion carried out in the ρ_L, ρ_T, θ_0 domain. Resistivity artefacts are observed in the ρ_L and ρ_T reconstructions. They are especially notable in the ρ_T model parameter, where a section of low resistivity is observed at depths between 5 and 10 m close to the left-hand side borehole. This region indicates that the inversion update has actually been in the wrong direction. The other noteworthy point is the large scale difference between the Cartesian and eigenframe inversions, especially for the θ_0 and ρ_{xz} parameters (see Fig. 12). Values for θ_0 are updated to magnitudes as high as 80°, though it is important to point out the region in which the high angle values occur corresponds to a region of relative isotropy. For an isotropic model the θ_0 angle has no real meaning because any angle will still satisfy isotropy. The data misfit converges to 12 per cent for the ρ_L, ρ_T, θ_0 inversion, compared to 2.25 per cent for the inversion in the ρ_{XX}, ρ_{XZ}, ρ_{ZZ} domain.

Fig. 14 shows an inversion reconstruction for a second model consisting of two anisotropic blocks in an otherwise isotropic background of 500 Ωm. The anisotropic targets both have $\rho_L = 300\,\Omega$ and $\rho_T = 700\,\Omega$ m, with the blocks having an axis of symmetry defined by $\theta_0 = +45^\circ$ (top block) and $\theta_0 = -45^\circ$ (bottom block). The coefficient of anisotropy was not extreme at $\lambda \sim 1.5$, so as to keep the non-uniqueness of the inversion to manageable levels. The inversion (damping factor of 0.0001 and 14 iterations) was carried out in the Cartesian frame as this produced the more accurate results in the previous experiment. After convergence, the model parameters were converted to the eigenframe for presentation. An isotropic starting model of $\rho_{XX} = \rho_{ZZ} = 500\,\Omega$m and

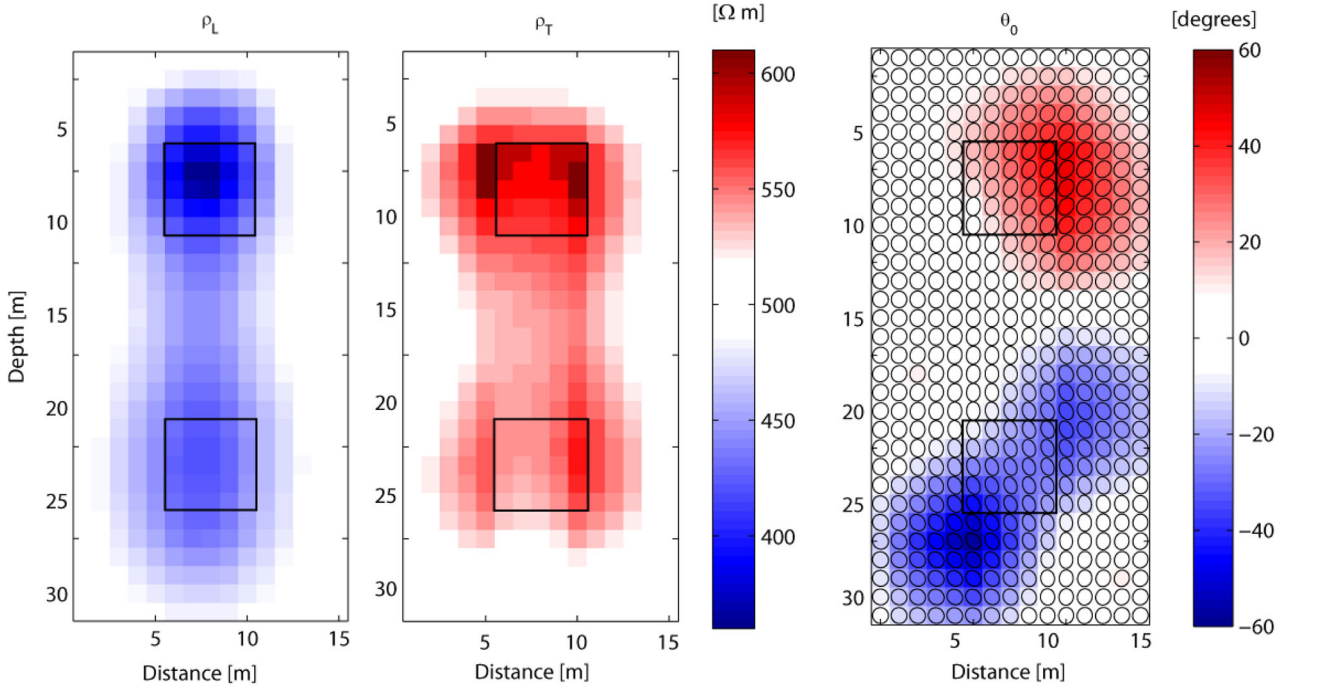

Figure 14. Three parameter inversion of anisotropic block in isotropic background. The block position is outlined in black. The true model parameters are: $\rho_L = 300\,\Omega$ and $\rho_T = 700\,\Omega$ m, with the target having an axis of symmetry defined by $\theta_0 = +45^\circ$. The inversion was carried out in the Cartesian co-ordinate frame and transformed back into the eigen (or rock) frame.

$\rho_{xz} = 0\,\Omega\,\mathrm{m}$ was employed. The reconstruction of the true targets in terms of resistivity values (ρ_{L} and ρ_{T}) and true locations is accurate for both cases. The model rms error is just 0.0025. Slight smearing effects are observed especially for the ρ_{T} parameter beneath the target away from the increased sensitivity of the surface electrodes.

The θ_0 reconstruction shows relatively poor spatial resolution of the target. The target angles themselves were well resolved, with angles of up to $+45^{\circ}$ recovered for the top block and -45° for the bottom block. Considerable smearing of the anomalies is apparent in both cases along the axes of symmetry directions. Despite these artefacts the inversion converged to a data misfit of below 2 per cent. This example is important because it illustrates the problems associated with non-uniqueness when inverting for the third model parameter: ρ_{xz} or θ.

5 CONCLUSIONS

We have conducted 2.5-D resistivity inversion experiments in TTI media. The synthetic data were computed for the true anisotropic models but the inversion scheme used forward solvers and sensitivity calculations for either the correct anisotropic assumption (two or three parameters at each cell defining the conductivity tensor) or the incorrect isotropic assumption (single conductivity value for each cell). This enabled direct comparison of the effect of the assumption (anisotropic vs isotropic) on the image constructions.

Synthetic models included isotropic targets embedded in a TI anisotropic background, as well as TI anisotropic blocks within an isotropic background, and in which the magnitude of anisotropy and the dip angle of the axis of symmetry were varied. These models were investigated through a series of experiments with varying orientation and magnitude of anisotropy. Superior reconstructions in terms of rms data misfit, the true anomaly shape and position, and the anisotropic background parameters were achieved when the correct anisotropic assumption was employed. When the false (but widely practised) isotropic assumption was used the tomograms were dominated by patterns of banded artefacts. For increasing levels of anisotropy, the isotropic reconstructions became increasingly poor, with high data misfits. For weakly anisotropic media, isotropic inversions performed adequately, especially for surface electrode arrays.

Various cross-hole data set types were investigated by examining the accuracy of the inversion result, the eigenspectra spectra of the pseudo-Hessian matrix and the relative resolution plots. The pole–dipole comprehensive data set produced the best reconstructions. However, we found that a data selection scheme based on using only the high sensitivity measurements produced tomograms of comparable quality to those of the comprehensive data sets, but involving far fewer measurements and hence reduced computer memory and run time.

Reconstruction experiments conducted with the simplistic inversion scheme were successfully extended to resolving three anisotropic parameters at each model cell (dip angle of the symmetry axis in addition to the transverse and longitudinal resistivities). For a layered anisotropic model with model parameters described in different co-ordinate frames (Cartesian and the eigenframe) the Cartesian frame provided a more accurate inversion results and a smaller rms data misfit. The eigenframe-based inversion instability was explained by means of the eigen-spectrum of the Hessian matrix which showed orders of magnitude difference between various parameters.

ACKNOWLEDGEMENTS

This research was supported by grants from the Australian Research Council and the Swiss National Science Foundation. We thank the Editor, Dr Rene-Edouard Plessix and the two anonymous reviewers for their constructive comments and suggestions to improve the manuscript.

REFERENCES

Al-Garnt, M. & Everett, M.E., 2003. The paradox of anisotropy in loop-loop electromagnetic response over a uniaxial halfspace, *Geophysics*, **68**, 892–899.

Asten, M.W., 1974. The influence of electrical anisotropy on mise a la masse surveys, *Geophys. Prospect.*, **22**, 238–245.

Athanasiou, E.N., Tsourlos, P.I. & Papazachos, C.B., 2009. Optimizing electrical resistivity array configurations by using a method based on the sensitivity matrix, in *Proceedings of the 15th EAGE Near Surface Meeting*, Dublin, Extended Abstract.

Bibby, H.M., Caldwell, T.G. & Brown, C., 2005. Determinable and non-determinable parameters of galvanic distortion in magnetotellurics, *Geophys. J. Int.*, **163**, 915–930.

Bhattacharya, P.K. & Patra, H.P., 1968. *Direct Current Geoelectric Sounding: Principles and Applications*, Elsevier.

Blome, M., 2009. Efficient measurement and data inversion strategies for large scale geoelectric surveys, *PhD thesis*, ETH, Zurich.

Blome, M., Maurer, H. & Greenhalgh, S.A., 2011. Geoelectric experimental design—efficient acquisition and exploitation of complete pole-bipole data sets, *Geophysics*, **76**, 15–26.

Busby, J.P., 2000. The effectiveness of azimuthal apparent resistivity measurements as a method for determining fracture strike orientations, *Geophys. Prospect.*, **48**, 677–698.

Butler, D. ed., 2005. *Near Surface Geophysics*, Society Exploration Geophysics.

Caldwell, T.G. & Bibby, H.M., 1998. The instantaneous apparent resistivity tensor: a visualisation scheme for LOTEM electric field measurements, *Geophys. J. Int.*, **135**, 817–834.

Collins, J.L., Everett, M.E. & Johnson, B., 2006. Detection of near surface horizontal anisotropy in a weathered metamorphic schist by transient electromagnetic induction, *Phys. Earth planet. Inter.*, **158**, 159–173.

Dekker, D.L. & Hastie, L.M., 1980. Magnetotelluric impedance of an anisotropic layered earth model, *Geophys. J. R. astr. Soc.*, **61**, 11–20.

deGroot-Hedlin, C. & Constable, S., 1990. Occam's inversion to generate smooth, two-dimensional models from magnetotelluric data, *Geophysics*, **55**, 1613–1624.

Dey, A. & Morrison, H.F., 1979. Resistivity modelling for arbitrarily shaped two-dimensional structures, *Geophys. Prospect.*, **27**, 106–136.

Doetch, J., Linde, N., Coscis, I., Greenhalgh, S. & Green, A., 2010. Zonation for 3D aquifer characterization based on joint inversions of multimethod crosshole geophysical data, *Geophysics*, **75**, 53–64.

Everett, M.E. & Constable, S.C., 1999. Electric dipole field over an anisotropic seafloor. Theory and approach to the structure of the 40MA Pacific Ocean lithosphere, *Geophys. J. Int.*, **136**, 41–56.

Gianzero, S., 1999. The paradox of anisotropy revisited, *The Log Analyst*, **40**(6), 485–491.

Greenhalgh, M., 2008. DC resistivity modelling and sensitivity analysis in anisotropic media, *PhD thesis*, Adelaide University.

Greenhalgh, S.A., Marescot, L., Zhou, B., Greenhalgh, M. & Wiese, T., 2009a. Electric potential and Fréchet derivatives for a uniform anisotropic medium with a tilted axis of symmetry, *Pure appl. Geophys.*, **166**, 673–699.

Greenhalgh, S.A., Wiese, T. & Marescot, L., 2010. Comparison of DC sensitivity patterns for anisotropic and isotropic media, *J. appl. Geophys.*, **70**, 103–112.

Greenhalgh, S.A., Zhou, B. & Green, A., 2006. Solutions, algorithms and inter-relations for local minimization search geophysical inversion, *J. geophys. Eng.*, **3**, 101–113.

Greenhalgh, S.A., Zhou, B., Greenhalgh, M., Marescot, L. & Wiese, T., 2009b. Explicit expressions for the Fréchet derivatives in 3D anisotropic resistivity inversion, *Geophysics*, **74**, 31–43.

Habberjam, G.M., 1975. Apparent resistivity, anisotropy and strike measurements, *Geophys. Prospect.*, **23**, 211–247.

Herwanger, J.V., Pain, C.C., Binley, A., de Oliveira, C.R.E. & Worthington, M.H., 2004. Anisotropic resistivity tomography, *Geophys. J. Int.*, **158**, 409–425.

Hill, D.G., 1972. A laboratory investigation of electrical anisotropy in Precambrian rocks, *Geophysics*, **37**, 1022–1038.

Keller, G.V. & Frischknecht, F.C., 1966. *Electrical Methods in Geophysical Prospecting*, Pergamon.

Kim, J., Yi, M., Cho, S., Son, J. & Song, W., 2006. Anisotropic crosshole resistivity tomography for ground safety analysis of a high-storied building over an abandoned mine, *J. Environ. Eng. Geophys.*, **11**, 225–235.

LaBreque, D.J., Heath, G., Sharpe, R. & Versteeg, R., 2004. Autonomous monitoring of fluid movement using 3-D electrical resistivity tomography, *J. Environ. Eng. Geophys.*, **9**, 167–176.

Lehmann, H., 1995. Potential representation by independent configurations on a multi-electrode array, *Geophys. J. Int.*, **120**, 331–338.

Le Masne, D. & Vasseur, G., 1981. Electromagnetic field of sources at the surface of a homogeneous halfspace with horizontal anisotropy: application to fissured media, *Geophys. Prospect.*, **29**, 803–821.

Li, Y. & Spitzer, K., 2005. Finite element resistivity modelling for three-dimensional structures with arbitrary anisotropy, *Phys. Earth planet. Inter.*, **150**, 15–27.

Linde, N. & Pedreson, L.B., 2004. Evidence of electrical anisotropy in limestone formations using the RMT technique, *Geophysics*, **69**, 909–916.

Loewenthal, D. & Landisman, M., 1973. Theory for magnetotelluric observation on the surface of a layered anisotropic half-spac, *Geophys. J. R. astr. Soc.*, **35**, 195–214.

Loke, M.H., Wilkinson, P.B. & Chambers, J.E., 2010. Fast computation of optimized electrode arrays for 2D resistivity surveys, *Comput. Geosci.*, **36**, 1414–1426.

Loke, M.H., Wilkinson, P.B., Chambers, J.E. & Strutt, M., 2014. Optimized arrays for 2D cross borehole electrical tomography surveys, *Geophys. Prospect.*, **62**, 172–189.

Lu, X., Alumbaugh, D.L. & Weiss, C.J., 2002. Electric fields and currents produced by induction logging instruments in anisotropic media, *Geophysics*, **67**, 478–483.

Maillet, R., 1947. The fundamental equations of resistivity prospecting, *Geophysics*, **12**, 529–556.

Matias, M.J.S., 2002. Square array anisotropy measurements and resistivity sounding interpretation, *J. appl. Geophys.*, **49**, 185–194.

Maurer, H. & Boerner, D., 1998. Optimized and robust experimental design: a non-linear application to EM sounding, *Geophys. J. Int.*, **132**, 458–468.

Maurer, H., Curtis, A. & Boerner, D., 2010. Recent advances in optimized geophysical survey design, *Geophysics*, **75**, 177–194.

Menke, W., 1989. *Geophysical Data Analysis: Discrete Inverse Theory*, Academic Press.

Pain, C., Herwanger, J., Saunders, J., Worthington, M. & de Oliveira, C., 2003. Anisotropic resistivity inversion, *Inverse Problems*, **19**, 1081–1111.

Parkomenko, E.I., 1967. *Electrical Properties of Rocks*, Plenum Press.

Reddy, I.K. & Rankin, D., 1971. Magnetotelluric effect of dipping anisotropies, *Geophys. Prospect.*, **19**, 84–97.

Reynolds, J.M., 2009. *Introduction to Applied and Environmental Geophysics*, 2nd edn, John Wiley.

Rubin, Y. & Hubbard, S. eds, 2005. *Hydrogeophysics*, Springer.

Slater, L., Sandberg, S.K. & Jankowski, M., 1998. Survey design procedures and data processing techniques applied to the EM azimuthal resistivity method, *J. Environ. Eng. Geophys.*, **3**, 167–177.

Stummer, P., Maurer, H. & Green, A., 2004. Experimental design: electrical resistivity data sets that provide optimum subsurface information, *Geophysics*, **69**, 120–139.

Stummer, P., Maurer, H. & Horstmeyer, H., 2002. Optimization of DC resistivity data acquisition: real-time experimental design and a new multielectrode system, *IEEE Trans. Geosci. Remote Sens.*, **40**, 2727–2735.

Wannamaker, P.E., 2005. Anisotropy versus heterogeneity in continental solid earth electromagnetic studies: fundamental response charactersistics and implications for physiochemical state, *Surv. Geophys.*, **26**, 733–765.

Wang, T. & Fang, S., 2001. 3-D electromagnetic anisotropy modelling using finite differences, *Geophysics*, **66**, 1386–1398.

Watson, K.A. & Barker, R.D., 1999. Differentiating anisotropy and lateral effects using azimuthal resistivity offset soundings, *Geophysics*, **64**, 739–745.

Weiss, C.J. & Newman, G.A., 2002. Electromagnetic induction in a fully 3D anisotropic earth, *Geophysics*, **67**, 1104–1114.

Wiese, T., Greenhalgh, S.A. & Marescot, L., 2009. DC resistivity sensitivity patterns for tilted transversely isotropic media, *Near Surf. Geophys.*, **7**, 125–139.

Wilkinson, P.B., Loke, M.H., Meldrum, P.I., Chambers, J.E., Kuras, O., Gunn, D.A. & Ogilvy, D., 2012. Practical aspects of applied optimized survey design for electrical resistivity tomography, *Geophys. J. Int.*, **189**, 428–440.

Wilkinson, P.B., Meldrum, P.I., Chambers, J.E., Kuras, O. & Ogilvy, R.D., 2006. Improved strategies for the automatic selection of optimized sets of electrical resistivity tomograph measurements configurations, *Geophys. J. Int.*, **167**, 1119–1126.

Xu, B. & Noel, M., 1993. On the completeness of data sets with multielectrode systems for electrical resistivity surveys, *Geophys. Prospect.*, **41**, 791–801.

Yi, M.J., Kim, J.H. & Chung, S.H., 2011. Three-dimensional anisotropic inversion of resistivity tomography data in an abandoned mine area, *Explor. Geophys.*, **42**, 7–17.

Yin, C. & Fraser, D., 2004. The effect of electrical anisotropy on the response of helicopter-borne frequency-domain electromagnetic systems, *Geophys. Prospect.*, **52**, 399–416.

Yu, L. & Edwards, N., 1992. The detection of lateral anisotropy of the ocean floor by electromagnetic methods, *Geophys. J. Int.*, **108**, 433–441.

Zhe, J.P., Greenhalgh, S. & Marescot, L., 2007. Multichannel full waveform and flexible electrode combination resistivity imaging system, *Geophysics*, **72**, 57–64.

Zhou, B. & Greenhalgh, S.A., 2000. Crosshole resistivity tomography using different electrode configurations, *Geophys. Prospect.*, **48**, 887–912.

Zhou, B., Greenhalgh, M. & Greenhalgh, S.A., 2009. 2.5D/3D resistivity modelling in anisotropic media using Gaussian quadrature grids, *Geophys. J. Int.*, **16**, 938–950.